Aeroacoustics Conferences
26-29 May 2026, Brussels, Belgium
32nd AIAA/CEAS Aeroacoustics Conference (2026)

10.2514/6.2026-3445

Turbulence Distortion Effects in Airfoil Leading-Edge Noise: Insights from Lattice Boltzmann Simulations

Sparsh Sharma*, Malav Soni†, Alexandre Suryadi‡ and Michaela Herr§
Institute of Aerodynamics and Flow Technology, German Aerospace Center (DLR), 38108 Braunschweig, Germany

Turbulence–airfoil interaction constitutes a primary broadband noise source in numerous aeroacoustic applications. Classical prediction frameworks, following Amiet's flat-plate model, assume that incoming turbulence convects to the leading edge without modification. The present work challenges this assumption by demonstrating, through high-fidelity lattice Boltzmann simulations of a NACA 0012 airfoil at chord-based Reynolds number $Re_c \approx 5.1 \times 10^5$ and free-stream Mach number $M = 0.059$, that the turbulence field undergoes a systematic, scale-dependent, and component-dependent transformation before impacting the airfoil surface. A distortion mapping operator $\mathcal{D}(\mathbf{k}, \theta)$ is introduced that relates the upstream spectral tensor Φ_{ij}^{∞} to the pre-impact tensor Φ_{ij}^{LE} in the stagnation region, with the non-dimensional wavenumber $\kappa = k\, r_{\mathrm{LE}}$ governing the transition between strong and weak distortion regimes. Reynolds-stress budgets and Lumley invariant trajectories reveal irreversible tensorial reorganisation of the turbulence state, including a transient eigenvalue reordering that cannot be captured by scalar or isotropic corrections. Patch-based spectral comparisons confirm that the mapping $\Phi^{\infty} \rightarrow \Phi^{\mathrm{LE}}$ is frequency-dependent and component-dependent, with wall-normal fluctuations preferentially suppressed at large scales ($\kappa \lesssim 1$) and cross-plane energy redistributed non-uniformly around the leading edge at smaller scales. These results establish turbulence distortion as a physically necessary pre-conditioning stage that must be accounted for explicitly in predictive models of leading-edge noise, rather than absorbed implicitly into acoustic transfer functions or empirical attenuation factors.

Nomenclature

c	=	Airfoil chord length
C_u, C_Λ	=	Empirical constants in grid-turbulence decay laws
d_g	=	Grid bar thickness
D	=	Distortion operator mapping $\Phi_\infty \rightarrow \Phi_{\mathrm{LE}}$
$E(k)$	=	One-dimensional kinetic-energy spectrum
f	=	Frequency
$G_i(\kappa)$	=	Component-wise spectral gain
k, k_x, k_y, k_z	=	Wavenumber and its Cartesian components
L_z	=	Airfoil span
L_p	=	Sound pressure level
M	=	Free-stream Mach number
M_g	=	Mesh size of turbulence-generating grid
p'	=	Fluctuating (acoustic) pressure
$\Psi_{pp}(\omega)$	=	Wall-pressure spectral density
Q	=	Second invariant of velocity-gradient tensor
Re_c	=	Chord-based Reynolds number
r_{LE}	=	Geometric leading-edge radius
St_c	=	Strouhal number $St_c = fc/U_\infty$

*Researcher, Institute of Aerodynamics and Flow Technology, German Aerospace Center (DLR), sparsh.sharma@dlr.de
†Researcher, Institute of Aerodynamics and Flow Technology, German Aerospace Center (DLR), malav.soni@dlr.de
‡Researcher, Institute of Aerodynamics and Flow Technology, German Aerospace Center (DLR), alexandre.suryadi@dlr.de
§Senior Researcher, Institute of Aerodynamics and Flow Technology, German Aerospace Center (DLR), michaela.herr@dlr.de

Tu	=	Turbulence intensity (%)
U_∞	=	Free-stream velocity
U_c	=	Scale-dependent convection velocity
$\mathbf{U}$	=	Mean velocity vector
$\mathbf{u}'$	=	Velocity fluctuation vector
Φ_∞	=	Upstream turbulence spectral tensor
Φ_{LE}	=	Near-leading-edge spectral tensor
$\Pi(\mathbf{k})$	=	Solenoidal projection tensor
y^+	=	Wall coordinate in viscous units
$\Gamma(\omega)$	=	Coherence weighting function
$\gamma^2(z,\omega)$	=	Spanwise coherence of wall pressure
Δt	=	LBM time step
Δx	=	LBM lattice spacing
κ	=	Dimensionless wavenumber $\kappa = k\, r_{\mathrm{LE}}$
ρ	=	Density
σ	=	Grid solidity (bar blockage ratio)
θ	=	Non-dimensional distortion parameter
ω_z	=	Spanwise vorticity component

I. Introduction

Leading-edge (LE) noise, generated by the interaction of incoming turbulence with an aerodynamic surface, constitutes one of the dominant broadband noise mechanisms in engineering systems ranging from wind turbines and cooling fans to aircraft propellers and rotorcraft [1, 2]. As trailing-edge and tonal noise sources have been progressively mitigated through geometric optimisation and flow control, the accurate prediction of inflow-turbulence noise has acquired increasing practical and scientific importance [3, 4].

The canonical framework for predicting LE noise was established by Amiet [1], who related the far-field acoustic pressure to the spectral content of the incoming turbulence through a linear transfer function derived for a semi-infinite flat plate. Central to this formulation is the assumption that turbulent eddies convect toward the leading edge as a frozen, spatially homogeneous field, without undergoing any modification by the mean flow in the stagnation region. While this assumption yields satisfactory predictions for thin airfoils at moderate Mach numbers, systematic discrepancies arise for finite-thickness geometries, particularly in the high-frequency regime where the turbulence wavelength becomes comparable to the leading-edge radius [5–7]. These discrepancies have been documented across both analytical extensions and numerical studies [8–13], and have been partially addressed by geometric corrections or empirical attenuation factors [2, 14, 15], yet a mechanistic explanation rooted in the physics of the turbulence transformation remained incomplete.

A growing body of evidence from analytical, experimental, and computational studies suggests that the missing mechanism is the distortion of turbulence in the stagnation region upstream of the leading edge, as illustrated in Fig. 1. As turbulent eddies approach the airfoil, they encounter strong velocity gradients arising from the mean stagnation flow. This strain field compresses structures in the wall-normal direction, stretches them tangentially, and redistributes turbulent kinetic energy between velocity components, producing an anisotropic and structurally modified turbulence state before acoustic scattering occurs. The theoretical basis for this process was established through rapid distortion theory (RDT) [16, 17], which describes the linear evolution of turbulence subjected to rapid mean-flow deformation. Goldstein and Atassi [17] showed that the response of an airfoil to an incoming gust is fundamentally altered when the mean-flow distortion of the gust is accounted for, a finding later extended to stagnation geometries by Hunt and Carruthers [18]. Semi-empirical approaches have attempted to account for this physics through streamline-based corrections to the incoming turbulence [3, 19–21], while experimental studies have provided complementary evidence of scale-dependent distortion [22, 23]. More recently, high-fidelity numerical simulations using lattice Boltzmann methods have enabled direct observation of the multi-scale distortion process in the pre-impact region [13, 24], confirming that large-scale eddies undergo partial blockage and energy redistribution, while smaller-scale structures are increasingly damped by local flow gradients. These observations collectively demonstrate that the incoming turbulence cannot be treated as an invariant input to the acoustic problem.

Despite this body of evidence, turbulence distortion has rarely been isolated as the primary object of modelling. In most existing frameworks, its effects enter implicitly through modifications to the acoustic response, streamline-based

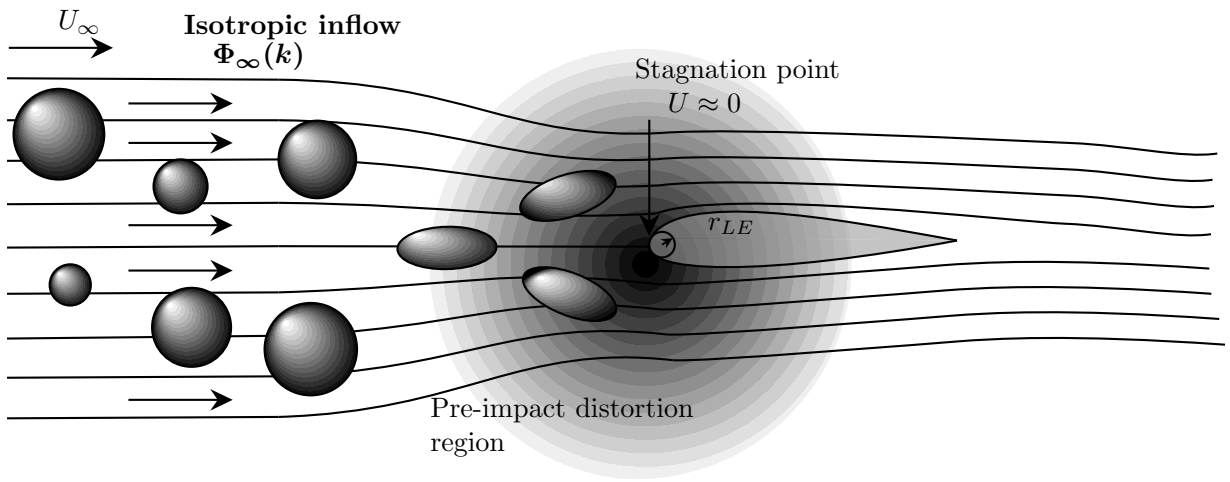

Fig. 1 Schematic illustration of pre-impact distortion of incoming turbulence near the leading edge.

input corrections, or fitted attenuation functions. Such treatments can improve prediction accuracy within specific parameter regimes but systematically obscure the pre-impact transformation of the turbulence field itself. As summarised in Fig. 2 and Tables 1–2, the literature has progressively moved from treating turbulence as an undistorted acoustic input toward recognising finite-thickness and stagnation-region effects, but an explicit and systematic characterisation of the turbulence transformation as a mapping between flow states has not been established.

The present work addresses this gap by introducing the concept of a *distortion mapping operator* $\mathcal{D}(\mathbf{k}, \theta)$, which directly relates the upstream spectral tensor Φ_{ij}^{∞} to the distorted pre-impact tensor Φ_{ij}^{LE} in the leading-edge region. Rather than modifying the acoustic scattering model, this approach characterises the transformation of the turbulence field that precedes and conditions the acoustic interaction. The operator framework is grounded in rapid distortion theory and evaluated against high-fidelity lattice Boltzmann simulation data of turbulence interacting with a NACA 0012 airfoil at $Re_c \approx 5.1 \times 10^5$. The principal objectives of this study are: (i) to quantify, through spectral analysis and statistical diagnostics, the transformation of the turbulence field between the upstream reference plane and the pre-impact region; (ii) to demonstrate that this transformation is scale-dependent, component-dependent, and geometrically organised by the leading-edge radius; and (iii) to establish that any predictive model of LE noise must explicitly account for this pre-conditioning stage.

The paper is structured as follows. Section II introduces the mathematical framework for turbulence distortion as an operator mapping. Section III describes the lattice Boltzmann solver and subgrid-scale modelling. Section IV presents the computational configuration and data acquisition strategy. Sections V–X present results on the flow-field evolution, Reynolds-stress redistribution, invariant diagnostics, and spectral distortion. Section XI summarises the findings and their implications for LE noise modelling.

II. Mathematical Framework: Turbulence Distortion as an Operator

A. Flow setting and spectral description

Consider a low-Mach, incompressible turbulent flow convecting toward an airfoil leading edge. Let $\Phi_{ij}^{\infty}(\mathbf{k}, \omega) \in \mathbb{R}^{3\times3}$ denote the upstream spectral tensor evaluated on a planar surface located upstream of the leading edge, and $\Phi_{ij}^{\mathrm{LE}}(\mathbf{k}, \omega)$ the corresponding tensor in the pre-impact region enclosing the leading edge. The spectral tensor satisfies

$$\int \Phi_{ij}(\mathbf{k}, \omega)\, \mathrm{d}\mathbf{k}\, \mathrm{d}\omega = \langle u_i u_j \rangle, \tag{1}$$

and encodes both the energy distribution and the anisotropy of the turbulence field across wavenumber and frequency. A local orthonormal frame (t, n, z) is adopted at the leading edge, corresponding to tangential, wall-normal, and spanwise directions, respectively.

Table 1 Classical and foundational studies on leading-edge noise.

Year	Authors	Category	Key Contribution	Limitation
1975	Amiet [1]	Analytical	Flat-plate LE noise model via linear transfer function	Assumes undistorted, frozen upstream turbulence
1976–79	Paterson & Amiet [5, 6]	Experimental	Identified high-frequency discrepancies for thick airfoils	No mechanistic explanation within model
1976	Goldstein & Atassi [17]	Analytical	RDT prediction of incoming gust deformation	Restricted to idealised geometries
1982	Olsen & Wagner [7]	Experimental	Airfoil thickness reduces high-frequency noise	Turbulence field upstream not characterised
1998–2011	Lockard, Hall et al. [8, 10]	Numerical / Analytical	Extended LE noise models to realistic geometries	Focus on acoustic response, not turbulence state
2010	Glegg & Devenport [2]	Analytical / Hybrid	Panel-method thickness corrections for turbulent inflow	Geometry-specific; distortion treated implicitly

Table 2 Modern developments and evidence of turbulence distortion effects.

Year	Authors	Category	Key Contribution	Relevance to Distortion
1997–2005	Guidati [19, 20]; Moriarty et al. [3, 21]	Semi-empirical	Streamline-based correction models for wind turbine noise	Distortion enters implicitly via velocity triangle
2004–2016	Gershfeld [14]; Lysak [15]; Kim et al. [4, 25]	Empirical / Analytical	High-frequency exponential thickness corrections	Captures integrated effect, not physical mechanism
2013	Gill et al. [22]	Experimental	Controlled gust–airfoil interaction, thickness effects	Demonstrates scale-dependent distortion directly
2022	Bowen et al. [23]	Experimental	Turbulence intensity and integral scale effects on LE noise	Highlights stagnation-region dynamics
2023–2024	dos Santos et al. [26]; Piccolo et al. [13]	Experimental / Numerical (LBM)	Direct observation of turbulence distortion near LE	Multi-scale evidence; distortion quantified from data
–	This work	Numerical (LBM)	Explicit operator framework $\Phi^{\infty} \rightarrow \Phi^{\mathrm{LE}}$	Distortion isolated as primary preconditioning stage

B. Distortion as an operator mapping

The central hypothesis of this work is that the leading-edge mean flow imposes a well-defined transformation on the turbulence spectral tensor. This is expressed as

$$\Phi_{ij}^{\mathrm{LE}}(\mathbf{k}, \omega) = \mathcal{D}_{ijmn}(\mathbf{k}, \theta)\, \Phi_{mn}^{\infty}(\mathbf{k}, \omega), \tag{2}$$

where $\mathcal{D}_{ijmn}$ is a fourth-order, scale- and orientation-dependent distortion tensor, and θ is a non-dimensional distortion parameter characterising the integrated strain experienced by a fluid parcel convecting from the upstream reference plane to the leading-edge vicinity. This formulation treats turbulence distortion as a transformation acting directly on the spectral tensor, rather than as a correction applied at the level of the acoustic transfer function, which is the approach taken by most existing models.

C. Structure of the operator

Guided by rapid distortion theory [16, 18], the operator $\mathcal{D}$ can be decomposed into two physically distinct contributions.

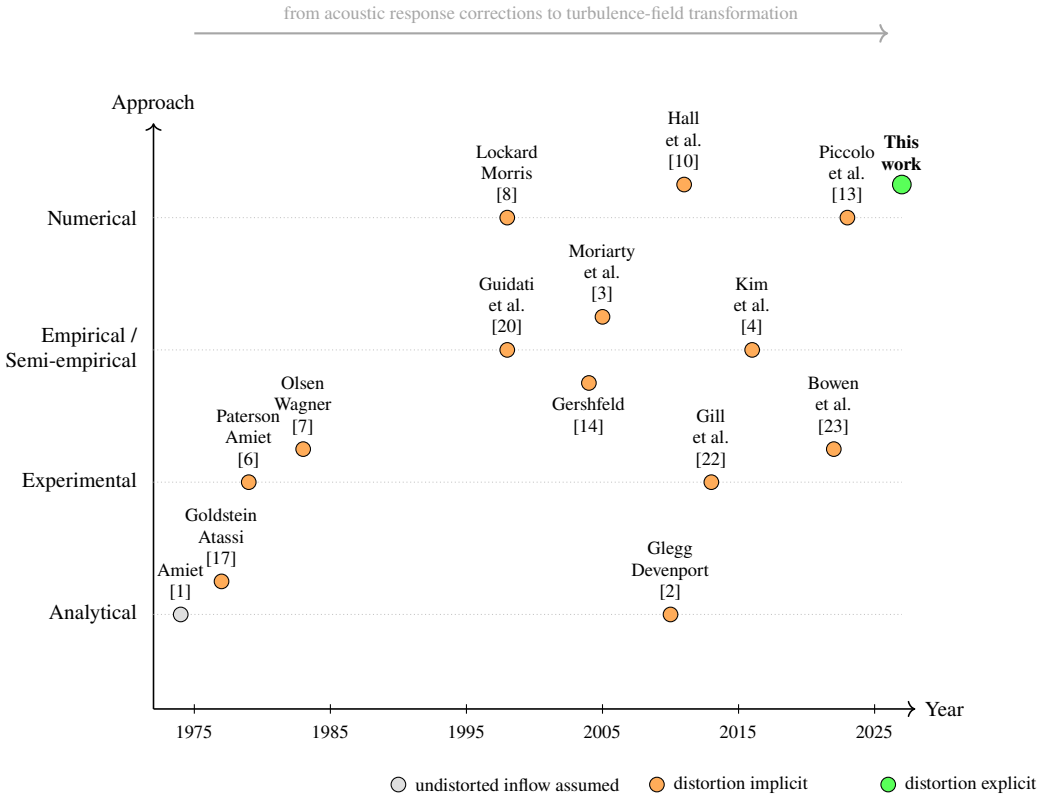

Fig. 2 Chronological evolution of leading-edge noise prediction approaches. Classical models treat the incoming turbulence as an undistorted acoustic input, while later analytical, experimental, empirical, and numerical studies increasingly reveal finite-thickness and stagnation-region distortion effects. The present work introduces an explicit mapping between upstream and near-leading-edge turbulence states.

Wavevector deformation. The mean stagnation flow deforms the material frame in which wavenumbers are defined. Under a local deformation gradient $F(\theta)$, wavevectors transform as

$$\mathbf{k} \;\mapsto\; \tilde{\mathbf{k}} = F^{-\top}(\theta)\,\mathbf{k}, \tag{3}$$

so that the support of the spectral tensor is redistributed in wavenumber space.

Component redistribution via solenoidal projection. Mass conservation requires that $\nabla \cdot \mathbf{u}' = 0$ is preserved throughout the distortion. This is enforced by the projection tensor

$$\Pi_{ij}(\mathbf{k}) = \delta_{ij} - \frac{k_i k_j}{\|\mathbf{k}\|^2}, \tag{4}$$

which projects the deformed velocity field back onto the solenoidal subspace. The resulting transformed spectral tensor takes the form

$$\mathcal{D}(\mathbf{k},\theta)\left[\Phi^{\infty}\right] \;\sim\; \Pi(\mathbf{k})\,F(\theta)\,\Phi^{\infty}(\tilde{\mathbf{k}},\omega)\,F^{\top}(\theta)\,\Pi(\mathbf{k}), \tag{5}$$

where $\tilde{\mathbf{k}} = F^{\top}(\theta)\mathbf{k}$ follows from Eq. (3). This expression is not employed here as a closed predictive model but rather as a structural guide for interpreting the observed transformations in the simulation data.

D. Scaling and non-dimensionalisation

The dominant non-dimensional parameter governing the distortion is the wavenumber ratio

$$\kappa = k\,r_{\mathrm{LE}}, \tag{6}$$

which compares the turbulent length scale to the geometric scale of the leading edge. For the deformation tensor associated with an idealised stagnation flow of strain rate a, the distortion parameter is $\theta = a\tau$, where τ is the convection time from the upstream reference plane to the leading edge. Two limiting regimes are expected from the operator structure:

- **Large-scale regime** ($\kappa \lesssim 1$): turbulent length scales exceed the leading-edge radius; these structures experience strong mean-flow deformation and undergo pronounced anisotropic energy redistribution.
- **Small-scale regime** ($\kappa \gg 1$): turbulent wavelengths are small relative to r_{LE}; the operator $\mathcal{D}$ approaches the identity and the pre-impact spectrum recovers the upstream characteristics.

E. Quantification from simulation data

The distortion operator is evaluated from data by comparing upstream and near-leading-edge spectral tensors. Component-wise amplification factors are defined as

$$G_q(f) = \frac{\Phi_{qq}^{\mathrm{LE}}(f)}{\Phi_{qq}^{\infty}(f)}, \qquad q \in \{u, v, w, p\}, \tag{7}$$

which provide a scale-resolved, diagonal representation of the transformation. Departures of G_q from unity quantify the amplitude of the distortion, while component-to-component differences in G_q quantify its tensorial (anisotropic) character. By analysing G_q as a function of κ, the existence of a universal collapse across operating conditions and the wavenumber structure of $\mathcal{D}$ can be assessed.

F. Scope and limitations

The present formulation focuses on the pre-impact transformation of the turbulence field and does not explicitly model the subsequent acoustic scattering. Nonlinear interactions, viscous effects, and the finite Mach-number correction to the frozen-flow approximation are not resolved within the operator, but are implicitly embedded in the simulation data from which G_q is extracted. The objective is not to establish a complete theoretical closure but to provide a mathematically consistent and physically interpretable framework for quantifying turbulence distortion as a mapping between flow states.

III. Numerical Method

A. Lattice Boltzmann formulation

High-fidelity simulations are carried out using the lattice Boltzmann method (LBM) implemented in the industrial solver ProLB (version 3.3.1) [27]. The LBM is particularly suited for aeroacoustic applications because it resolves both unsteady hydrodynamic structures and acoustic wave propagation within a single, unified time-domain framework [28]. The discrete evolution of particle distribution functions $f_i(\mathbf{x}, t)$ is governed by

$$f_i(\mathbf{x} + \boldsymbol{\xi}_i \Delta t,\ t + \Delta t) = f_i(\mathbf{x}, t) + \Omega_i(\mathbf{x}, t), \tag{8}$$

where $\boldsymbol{\xi}_i$ are the discrete lattice velocities and Ω_i is the collision operator. Macroscopic density ρ and momentum $\rho\mathbf{u}$ are recovered from the zeroth and first moments of f_i, respectively. A hybrid recursive regularised BGK collision model is employed to ensure numerical stability at high Reynolds numbers while preserving accurate resolution of the turbulent fluctuations relevant to aeroacoustic source mechanisms.

B. Turbulence and wall modelling

Subgrid-scale effects are represented through a large-eddy simulation (LES) formulation with an effective kinematic viscosity

$$\nu_{\mathrm{eff}} = \nu + \nu_{\mathrm{turb}}, \tag{9}$$

where ν_{turb} is computed using a Smagorinsky-type closure with dynamic determination of the model coefficient [29]. Near-wall effects are handled via a logarithmic wall model applied at the first off-wall cell, incorporating corrections for streamwise pressure gradients and wall curvature. The resulting first-cell-centre height satisfies $y^+ = O(1)$ in the stagnation region, ensuring adequate resolution of the surface pressure dynamics relevant to acoustic source identification [30].

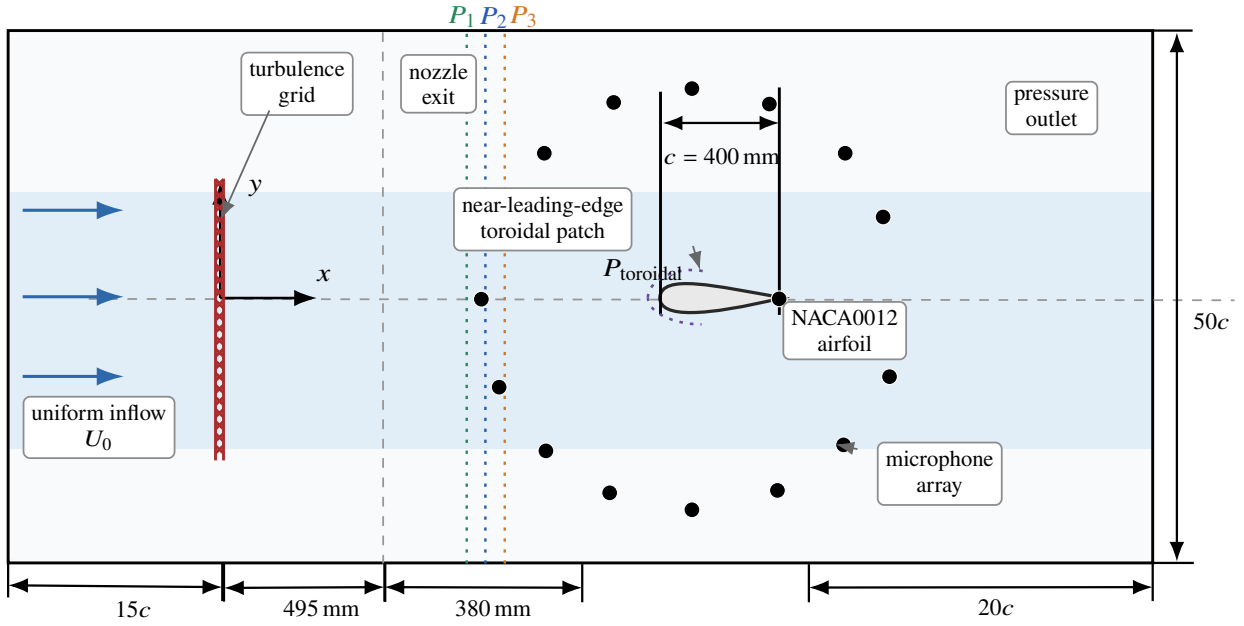

Fig. 3 Side view of the computational configuration. A passive turbulence-generating grid is positioned at $x = 0$ upstream of a NACA 0012 airfoil with its leading edge at $x/c = 1.875$. The two sampling regions used for the distortion analysis are indicated schematically.

C. Resolution considerations

The lattice spacing and time step are selected to resolve turbulent scales in the range $\kappa = O(1)$, i.e., those for which the distortion is expected to be most significant. Near the leading edge, the mesh is locally refined to capture the strong curvature and stagnation-region velocity gradients, while a coarser but dynamically consistent resolution is maintained in the far field. The short convection time between the upstream sampling plane and the pre-impact region justifies the neglect of large-scale nonlinear evolution, so that the observed spectral transformation can be attributed primarily to the interaction with the mean stagnation flow.

IV. Computational Setup and Data Acquisition

A. Computational configuration

The computational domain consists of a passive turbulence-generating grid positioned upstream of a NACA 0012 airfoil at zero geometric angle of attack. A schematic of the configuration is shown in Fig. 3. The turbulence-generating grid is located at $x = 0$, and the airfoil leading edge at $x = 0.875$ m. The airfoil chord length is $c = 0.4$ m, the span $L_z = 0.8$ m, and the leading-edge radius $r_{\text{LE}} \approx 6.3$ mm.

The free-stream velocity is $U_\infty = 20$ m/s, corresponding to a free-stream Mach number $M \approx 0.059$ and a chord-based Reynolds number $Re_c = U_\infty c/\nu \approx 5.1 \times 10^5$. The domain extends sufficiently far upstream and downstream to allow turbulence development and acoustic wave propagation. Non-reflecting boundary conditions and sponge layers are applied at all far-field boundaries to suppress spurious reflections.

B. Turbulence generation and inflow characterisation

Turbulence is generated by the passive grid placed upstream of the airfoil. The separation between the grid and the airfoil leading edge is chosen such that the turbulence field reaches a statistically developed state before interaction, while retaining sufficient large-scale energy in the range $\kappa \lesssim 1$ that is most relevant to the distortion process. The resulting inflow turbulence intensity at the upstream sampling plane is characterised in Section VI.

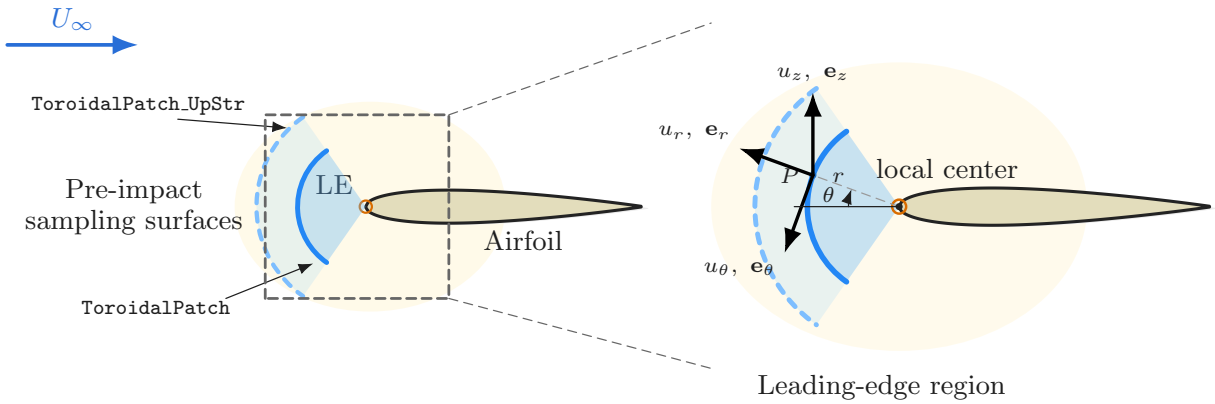

Fig. 4 Sampling regions used for distortion analysis. The planar upstream patch (`ToroidalPatch_UpStr`) provides the reference spectral tensor Φ^{∞}, while the toroidal surface (`ToroidalPatch`) enclosing the leading edge captures the distorted pre-impact tensor Φ^{LE}.

C. Sampling strategy for distortion analysis

Direct quantification of the distortion operator requires consistent measurements of the turbulence field at two locations: an upstream reference plane and a pre-impact surface enclosing the leading edge. The two sampling regions are illustrated in Fig. 4.

- **Upstream reference plane:** A planar sampling surface located one leading-edge radius upstream of the airfoil leading edge. Velocity time series acquired on this plane provide the reference spectral tensor Φ^{∞}_{ij}.
- **Pre-impact toroidal surface:** A surface following the nose geometry of the airfoil, enclosing the leading-edge region. This surface captures the distorted turbulence state Φ^{LE}_{ij} prior to acoustic interaction with the surface.

Velocity time series are recorded at all sampling points and decomposed in a local coordinate system aligned with the airfoil surface. Spectral tensors are estimated using the Welch method [31] with Hanning windowing and 50% overlap.

D. Data processing and spectral estimation

Spectral tensors at both locations are estimated from time series of sufficient duration to ensure convergence of the spectral estimators, with a frequency resolution $\Delta f = U_\infty/(10c)$ set to resolve the energetically significant range $St_c \in [0.1,\ 200]$. The convection velocity $U_c(f)$ is estimated from the phase of the streamwise cross-spectrum between adjacent upstream probes and used to relate temporal and spatial spectral representations where required [32].

V. Flow-Field Evolution and Reynolds-Stress Redistribution

A. Global flow organisation

The interaction between grid-generated turbulence and the airfoil is characterised through instantaneous and mean velocity fields, Reynolds stresses, and spanwise vorticity, as summarised in Fig. 5.

In the near-grid region, the instantaneous velocity field (Fig. 5(a)) exhibits distinct jet-like wakes and shear layers characteristic of passive grid-generated turbulence [33]. These structures progressively break down through nonlinear interactions, yielding a spatially decorrelated broadband turbulent field further downstream. Approaching the airfoil, however, a qualitative transition occurs: the turbulence undergoes visible reorganisation manifested as suppression of large coherent structures and emergence of finer, elongated features aligned with the local mean flow. This transition is not merely the continuation of free-space decay, but reflects the onset of mean-flow-induced distortion.

The mean velocity field (Fig. 5(b)) reveals the underlying mechanism. A pronounced stagnation region forms directly upstream of the leading edge, with strong acceleration of fluid around the nose. This configuration establishes a local strain field of the form

$$S_{ij} = \tfrac{1}{2}\left(\partial_i \overline{U}_j + \partial_j \overline{U}_i\right) \ \approx\ \mathrm{diag}(+a,\ -a,\ 0), \tag{10}$$

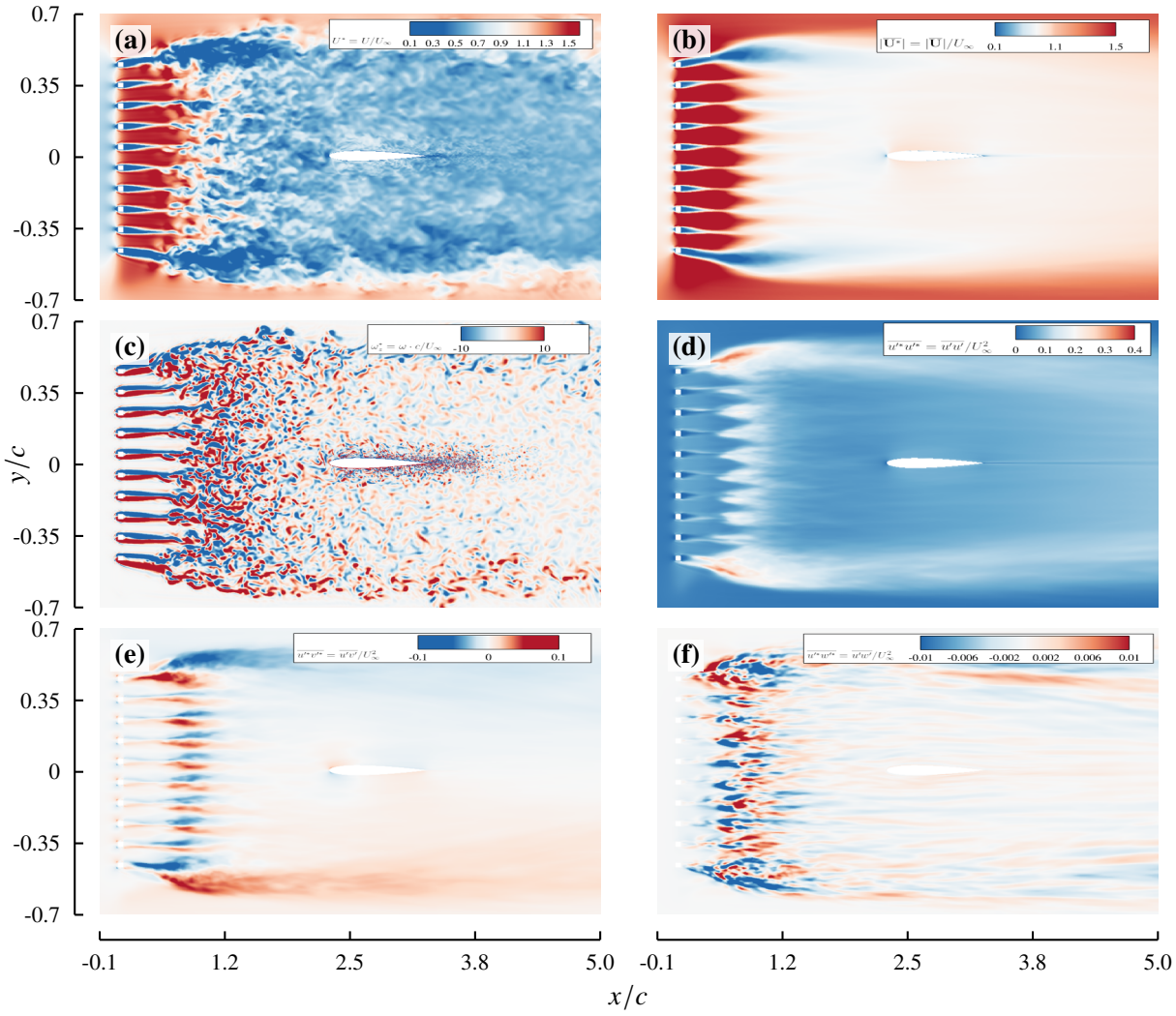

Fig. 5 Flow-field organisation downstream of the turbulence-generating grid and around the NACA 0012 airfoil: (a) instantaneous normalised velocity magnitude $|\mathbf{U}|/U_\infty$; (b) mean normalised velocity magnitude $|\overline{\mathbf{U}}|/U_\infty$; (c) instantaneous spanwise vorticity $\omega_z c/U_\infty$; (d) streamwise Reynolds stress $\overline{u'u'}/U_\infty^2$; Reynolds shear stress (e) $\overline{u'v'}/U_\infty^2$ and (f) $\overline{u'w'}/U_\infty^2$.

corresponding to streamwise extension and wall-normal compression. This is precisely the canonical stagnation-flow configuration studied in rapid distortion theory [16, 18], and constitutes the dominant mechanism by which the incoming turbulence is structurally modified prior to impact.

B. Reynolds-stress redistribution

The Reynolds-stress distributions shown in Figs. 5(d–f) quantify the consequences of the stagnation strain field. In the grid wake, the streamwise component $\overline{u'u'}$ is strongly dominant, consistent with the persistent large-scale anisotropy characteristic of passive-grid turbulence [33, 34]. Approaching the leading edge, $\overline{u'u'}$ decreases markedly while the shear stress $\overline{u'v'}$ develops a spatially organised structure with sign changes across the symmetry plane, reflecting the interaction of streamwise fluctuations with wall-normal mean-velocity gradients. The cross component $\overline{u'w'}$, shown in Fig. 5(f), reveals that this redistribution is not confined to the streamwise–wall-normal plane. Immediately downstream of the grid, $\overline{u'w'}$ exhibits alternating positive and negative regions associated with the separated wakes of the grid bars. This behaviour is important because it shows that the incoming turbulence is not distorted in a purely two-dimensional manner. Although the mean stagnation field is primarily organised in the streamwise–wall-normal plane, the finite-span

turbulent structures generated by the grid retain spanwise correlations that are modified during convection toward the leading edge.

This redistribution is a direct prediction of rapid distortion theory, in which the production tensor

$$P_{ij} = -R_{ik}\frac{\partial \overline{U}_j}{\partial x_k} - R_{jk}\frac{\partial \overline{U}_i}{\partial x_k} \tag{11}$$

couples the Reynolds stresses through the mean velocity-gradient field. In the present stagnation region this gradient is dominated by the symmetric strain component, with streamwise extension and wall-normal compression.Wall-normal compression ($-a$ in the y-direction) amplifies $\partial u/\partial y$ gradients and enhances pressure–strain redistribution toward v' fluctuations, while the extensional strain in x acts to suppress the streamwise component [16, 35]. Analogous behaviour has been documented in numerical studies of turbulence–airfoil interaction [8, 13].

C. Vorticity dynamics and shear-layer formation

The spanwise vorticity field (Fig. 5(c)) corroborates and extends this picture. In the upstream region, ω_z exhibits disordered, multi-scale structures arising from the breakdown of grid wakes. As the flow approaches the leading edge, the vorticity field transitions to thin, high-intensity shear layers aligned with the stagnation streamlines. This intensification arises from the compression-induced amplification of the wall-normal gradient $\partial u/\partial y$ in

$$\omega_z = \frac{\partial v}{\partial x} - \frac{\partial u}{\partial y}, \tag{12}$$

leading to concentration of vorticity into narrow regions. This transition from volumetric, isotropic vorticity to shear-dominated, coherent layers is a hallmark of rapid distortion in non-uniform mean flows [17, 18].

D. Implications for leading-edge noise

Taken together, the velocity, Reynolds-stress, and vorticity fields establish a consistent physical picture: the turbulence field undergoes a systematic mean-flow-induced transformation as it approaches the leading edge, producing an anisotropic pre-impact state that is qualitatively different from the upstream inflow. Since leading-edge noise is driven primarily by the wall-normal velocity fluctuation component interacting with the airfoil surface [1, 2], the observed redistribution of energy toward v' at intermediate and large scales, combined with the formation of coherent shear layers, will directly modify the effective acoustic forcing. These results motivate the operator formulation of Section II and provide the physical context for the spectral analysis that follows.

VI. Midspan Inflow Turbulence: Intensity, Coherence, and Spectra

A. Streamwise coordinate and mean-flow reference

Midspan statistics are extracted along a one-dimensional probe line at fixed (y, z), parameterised by

$$x^\star = \frac{x - x_{\mathrm{LE}}}{c}, \tag{13}$$

so that $x^\star = 0$ corresponds to the leading edge and the interval $0 \le x^\star \le 1$ is masked (solid airfoil body). Time-averaged and fluctuating quantities are defined as

$$\overline{u_i}(x) = \frac{1}{T}\int_0^T u_i(x,t)\,\mathrm{d}t, \qquad u_i'(x,t) = u_i(x,t) - \overline{u_i}(x), \tag{14}$$

with $i \in \{1, 2, 3\}$ corresponding to (u, v, w).

The mean streamwise velocity $\overline{u}$ shown in Fig. 6 increases monotonically toward the stagnation point, consistent with the acceleration of fluid around the leading edge. The transverse components $\overline{v}$ and $\overline{w}$ remain negligible along the midspan probe, confirming that convection along the probe line is primarily streamwise. It is emphasised, however, that $\overline{u}$ cannot be directly interpreted as a universal convection velocity for all turbulent scales; in inhomogeneous turbulence, U_c is known to be scale-dependent and generally differs from the local mean [32, 36, 37].

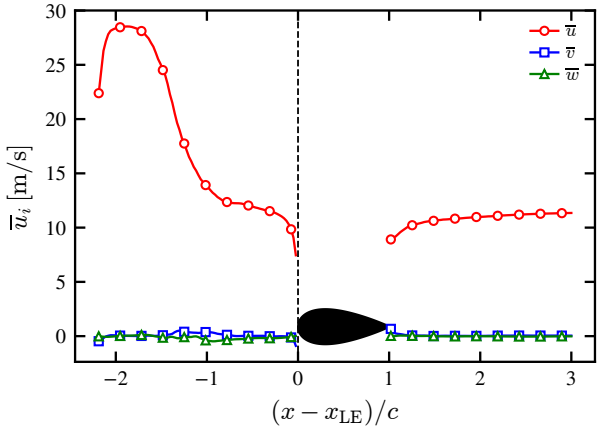

Fig. 6 Midspan mean velocity profiles along $x^\star = (x - x_{\mathrm{LE}})/c$. The solid-body interval $0 \le x^\star \le 1$ is masked and shown as the NACA 0012 contour.

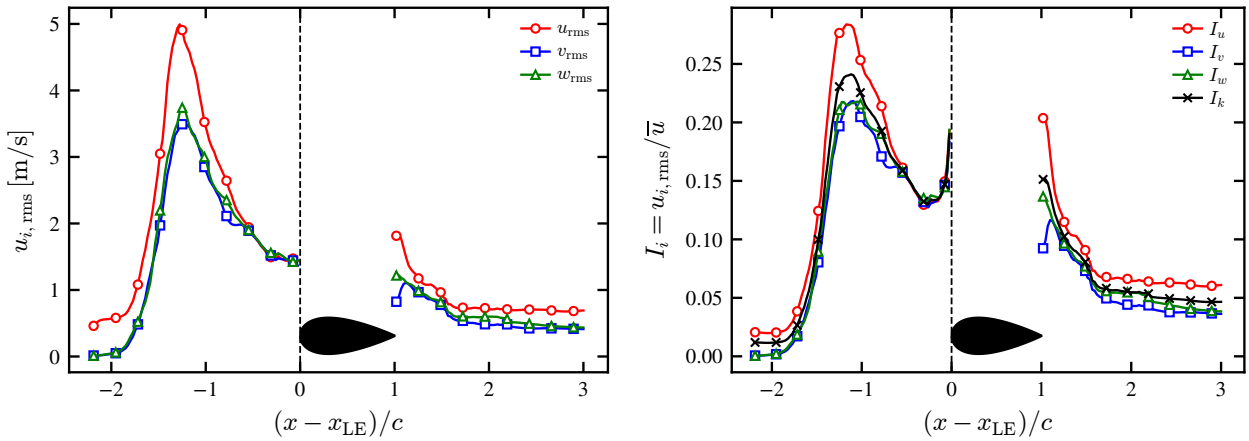

(a) **(b)**

Fig. 7 Midspan turbulence characteristics along $x^\star$: (a) component-wise root-mean-square velocity fluctuations; (b) turbulence intensities I_u, I_v, I_w and $I_k = \sqrt{2k/3}/|\overline{u}|$. The airfoil body is masked.

B. Fluctuation amplitudes and turbulence intensity

Fluctuation amplitudes are quantified through the Reynolds stresses

$$R_{ij}(x) = \overline{u_i'(x,t)\,u_j'(x,t)}, \qquad u_{i,\mathrm{rms}}(x) = \sqrt{R_{ii}(x)}, \tag{15}$$

and turbulence intensities

$$I_i(x) = \frac{u_{i,\mathrm{rms}}(x)}{|\overline{u}(x)|}, \qquad I_k(x) = \frac{\sqrt{2k(x)/3}}{|\overline{u}(x)|}, \quad k = \tfrac{1}{2}R_{ii}, \tag{16}$$

as shown in Fig. 7.

The streamwise component u_{rms} dominates throughout the domain, with $u_{\mathrm{rms}} > v_{\mathrm{rms}} \approx w_{\mathrm{rms}}$, confirming persistent large-scale anisotropy characteristic of passive-grid turbulence [33, 38]. The turbulence intensity profiles exhibit a pronounced upstream peak followed by non-monotonic evolution toward the leading edge, reflecting the superposition of free-space decay and the onset of mean-flow-induced distortion. This spatial non-uniformity has an important modelling consequence: the inflow cannot be represented by a single homogeneous turbulence state characterised by a scalar intensity, as is assumed in many semi-empirical prediction tools [3]. Furthermore, the preservation of the anisotropy ordering $I_u > I_v \approx I_w$ along the entire probe is consistent with the classical separation between large-scale anisotropy and small-scale isotropy in turbulent flows [39].

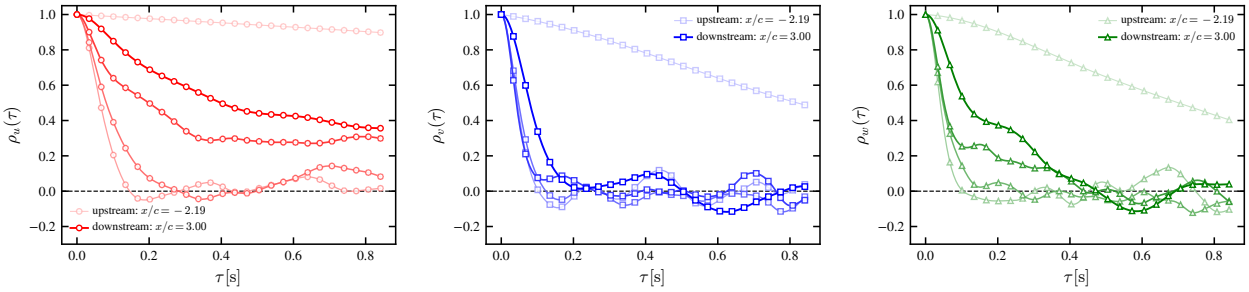

(a) $\rho_u(\tau)$ **(b)** $\rho_v(\tau)$ **(c)** $\rho_w(\tau)$

Fig. 8 Temporal autocorrelation functions $\rho_{u_i}(\tau; x_n)$ at multiple midspan stations.

C. Temporal coherence and integral time scales

The Eulerian autocorrelation function

$$\rho_{u_i}(\tau; x) = \frac{\overline{u_i'(x,t)\, u_i'(x,t+\tau)}}{\overline{u_i'^2}(x)}, \qquad \rho_{u_i}(0; x) = 1, \tag{17}$$

is shown for representative stations in Fig. 8.

Far upstream ($x^\star \approx -2.19$), all components decay slowly and monotonically, indicating long-coherence large-scale structures characteristic of near-grid turbulence [33]. Downstream of the airfoil ($x^\star = 3.0$), a rapid initial decay is followed by oscillatory behaviour about zero, reflecting the coexistence of fine-scale broadband content and quasi-periodic spectral signatures inherited from discrete grid shedding frequencies [33]. The streamwise component ρ_u retains a higher positive correlation level at large τ compared to ρ_v and ρ_w, indicating that temporal coherence is anisotropic and that elongated streamwise structures persist beyond the decorrelation of transverse components [39]. The superposition of rapid small-scale decorrelation with finite large-scale coherence confirms the multi-scale character of the turbulence field, which cannot be adequately represented by a single exponential correlation model.

D. Spatial coherence and one-dimensional wavenumber spectra

The streamwise two-point correlation

$$R_{u_i u_i}(r_x) = \frac{\langle u_i'(x,t)\, u_i'(x+r_x,t)\rangle}{\langle u_i'^2\rangle}, \qquad R_{u_i u_i}(0) = 1, \tag{18}$$

and the corresponding one-dimensional wavenumber spectrum (via the Wiener–Khinchin theorem)

$$E_{u_i u_i}(k_x) = \frac{1}{2\pi} \int_{-\infty}^{\infty} R_{u_i u_i}(r_x)\, e^{-ik_x r_x}\, \mathrm{d}r_x, \tag{19}$$

are shown in Fig. 9.

The measured correlations exhibit a sharp initial decay over short separations, followed by weak oscillatory tails consistent with quasi-periodic grid-induced signatures [33]. The streamwise correlation R_{uu} retains positive values over longer separations than R_{vv} and R_{ww}, confirming anisotropic spatial coherence with elongated streamwise structures [39, 40]. The wavenumber spectra are dominated at low k_x by the streamwise component, while the three components progressively collapse at high k_x, consistent with the recovery of local isotropy at small scales [39]. This gradual, rather than abrupt, transition across wavenumbers implies that anisotropy is distributed across a finite spectral band, reinforcing the need for a wavenumber-dependent distortion description.

E. Implications for distortion modelling

The midspan analysis places three direct constraints on any viable distortion operator. First, the spatial non-uniformity of the inflow precludes a homogeneous-turbulence approximation. Second, the persistence of anisotropy requires a tensorial treatment of the upstream spectral state. Third, the gradual spectral transition between anisotropic and

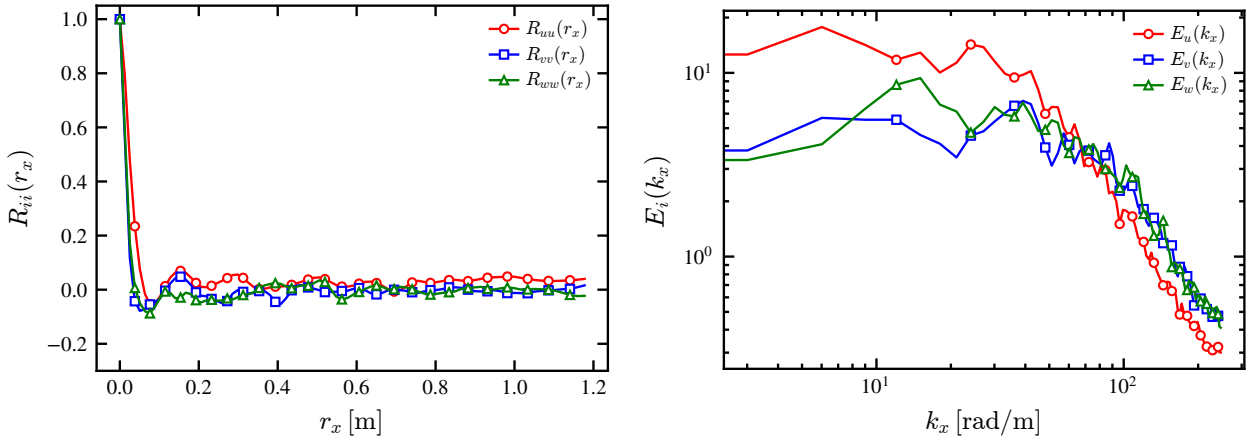

(a) Normalised spatial correlations $R_{u_iu_i}(r_x)$. **(b) 1D streamwise wavenumber spectra $E_{u_iu_i}(k_x)$.**

Fig. 9 Spatial coherence and wavenumber spectral content along the midspan probe.

quasi-isotropic regimes necessitates a wavenumber-dependent operator with distinct behaviour for $\kappa \ll 1$ and $\kappa \gg 1$. An additional modelling consideration arises from the scale dependence of the convection velocity, which must be properly accounted for when interpreting spectral mappings from temporal to wavenumber representations [32].

VII. Reynolds-Stress Evolution and Invariant Diagnostics

A. Reynolds-stress evolution along the midspan probe

The streamwise evolution of the Reynolds-stress tensor components is shown in Fig. 10(a). Far upstream ($x^\star \lesssim -1.5$), the turbulence is strongly anisotropic with

$$R_{11} \gg R_{22} \approx R_{33}, \tag{20}$$

a configuration arising from the preferential alignment of energy with the streamwise direction in passive-grid turbulence [33]. Approaching the leading edge, all normal stresses undergo rapid amplification with a pronounced peak near $x^\star \approx -0.2$. The production tensor (Eq. 11) evaluated under the stagnation strain (Eq. 10) shows that the dominant extensional direction aligns with u, so that R_{11} grows preferentially in the initial amplification phase. However, the critical observation is that the ratios between components change significantly as $x^\star \to 0$: the distortion is not a scalar amplification, but a genuine tensorial reorganisation. Downstream of the airfoil ($x^\star > 1$), all components decay sharply, but the relative ordering does not revert to the upstream state, demonstrating that the interaction acts as an irreversible transformation in stress space.

B. Invariant representation of the anisotropy state

To isolate structural changes in the turbulence from amplitude effects, the anisotropy tensor is defined as

$$b_{ij}(x) = \frac{R_{ij}(x)}{2k(x)} - \frac{1}{3}\delta_{ij}, \tag{21}$$

with scalar invariants

$$II = -\tfrac{1}{2}\, b_{ij}b_{ji}, \qquad III = \tfrac{1}{3}\, b_{ij}b_{jk}b_{ki}. \tag{22}$$

The trajectory in Lumley invariant space [41, 42] is shown in Fig. 10(b). Upstream, the data lie close to the axisymmetric contraction boundary, approaching the one-component limit, consistent with the dominance of R_{11} in Eq. (20).

As the flow approaches the leading edge, the trajectory moves systematically toward the origin, indicating a reduction in anisotropy magnitude ($\|b\|^2 \sim -2\,II$). However, the trajectory is not monotonic: a distinct lateral excursion is observed in which points deviate from the contraction boundary toward the expansion side ($III < 0$), implying a transient reordering of the principal components of the anisotropy tensor. Here λ_i denote the eigenvalues of b_{ij}, ordered

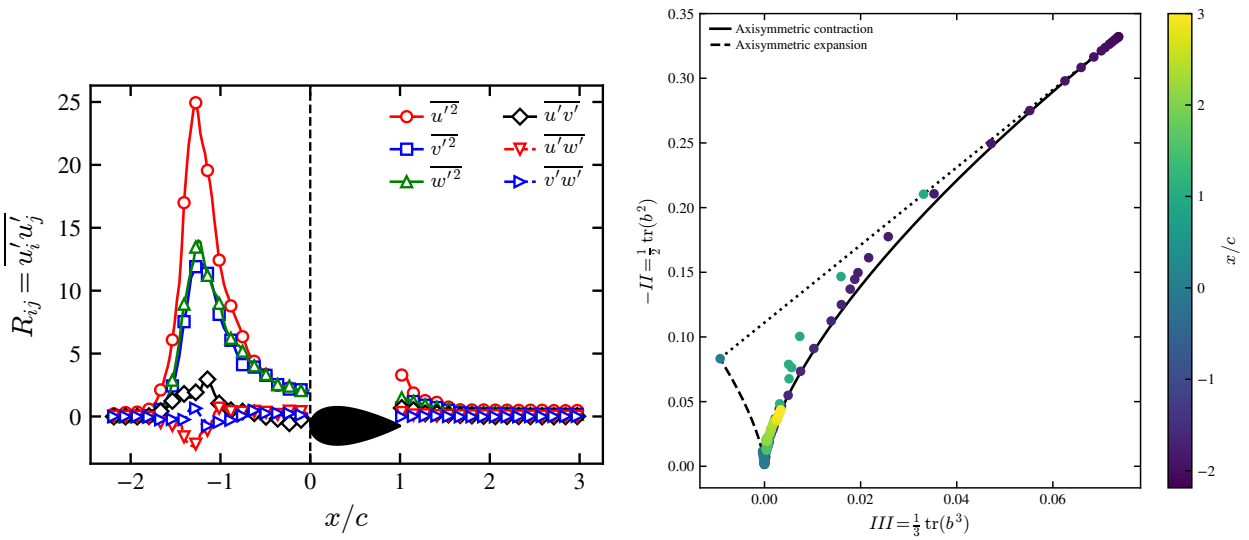

(a) **(b)**

Fig. 10 Midspan turbulence diagnostics along $x^\star = (x - x_{\mathrm{LE}})/c$: (a) Reynolds-stress components $R_{ij} = \overline{u_i' u_j'}$, showing upstream anisotropy, rapid pre-impact amplification, and post-passage attenuation with modified component ratios; (b) trajectory in Lumley invariant space $(III, -II)$, illustrating the transition from a near one-component, contraction-dominated state toward reduced anisotropy, with a transient excursion toward the expansion side ($III < 0$) indicating eigenvalue reordering. The solid-body interval $0 \le x^\star \le 1$ is masked.

such that $\lambda_1 \ge \lambda_2 \ge \lambda_3$:

$$\lambda_1 \approx \lambda_2 > \lambda_3. \tag{23}$$

before the state returns toward contraction-dominated configurations. This branch switching is the key structural finding: it demonstrates that the leading-edge interaction modifies not only the intensity of turbulence but its topology in eigenvalue space. Such behaviour arises from pressure–strain redistribution and finite-time nonlinear effects during the rapid distortion process [35, 43], and is not reproducible by linear scaling or isotropic corrections. Downstream, the trajectory remains closer to the isotropic point than upstream, confirming that the distortion leaves a persistent structural imprint.

C. Interpretation within the operator framework

In invariant space, the action of $\mathcal{D}(\mathbf{k}, \theta)$ corresponds to a systematic reduction of $-II$ (partial isotropisation) combined with a curvature of the trajectory governed by the relative rates of component amplification. The initial motion along the axisymmetric contraction boundary is consistent with a dominant extensional strain acting on a highly anisotropic upstream state, as predicted by the linear RDT operator (Eq. 5). The subsequent excursion toward $III < 0$ signals a deviation from idealised linear behaviour, attributable to pressure–strain interactions not captured by Eq. (5) in its simplest form. The invariant trajectory thus provides a compact, data-driven representation of $\mathcal{D}$, with the trajectory curvature encoding deviations from linear RDT predictions. For aeroacoustic modelling, the critical implication is clear: since LE noise depends sensitively on the wall-normal and correlated velocity fluctuations, any predictive framework must account for this full structural transformation, not merely the upstream energy content.

VIII. Spanwise Vorticity Evolution in Physical Space

The physical-space evolution of turbulence distortion is visualised through instantaneous spanwise vorticity fields at selected streamwise stations between the turbulence-generating grid and the airfoil leading edge, shown in Fig. 11.

At stations well upstream of the leading edge, ω_z exhibits approximately isotropic, spatially decorrelated multi-scale structures arising from grid-wake breakdown, consistent with classical observations of homogeneous grid turbulence [33]. Progressing downstream, eddies elongate in the streamwise direction and contract in the wall-normal direction under the

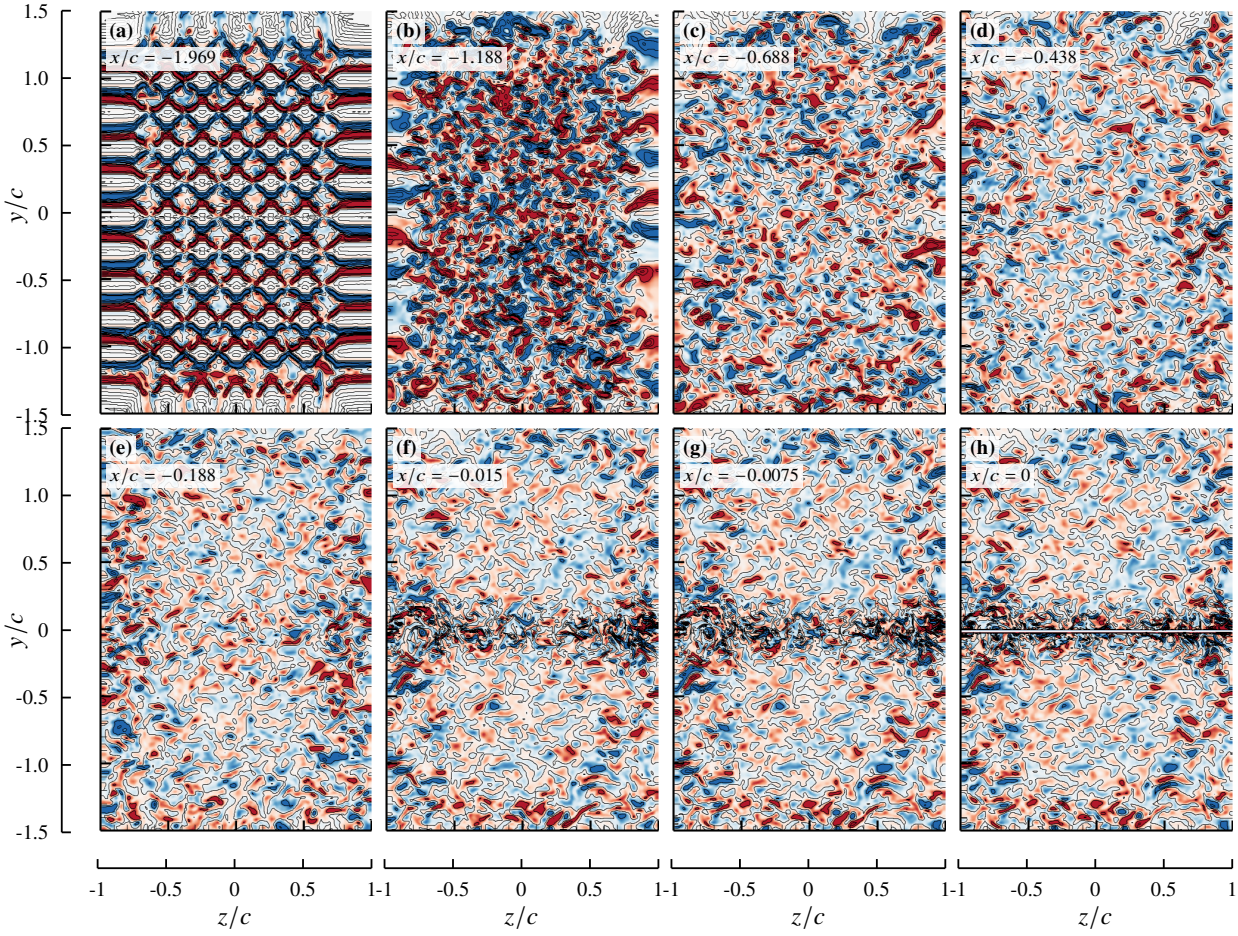

Fig. 11 Instantaneous spanwise vorticity $\omega_z c/U_\infty$ at eight streamwise stations progressing from far upstream to the leading edge of the airfoil. The displayed streamwise locations are shifted according to $(x - 0.875)/0.4$, so that the leading edge corresponds to $x/c = 0$. Only the first column carries the y/c axis, and only the bottom row carries the z/c axis.

action of the stagnation strain field (Eq. 10), a pattern fully consistent with RDT predictions for stagnation flows [17, 18]. In the immediate vicinity of the leading edge, the vorticity field is dominated by thin, intense shear layers aligned with the stagnation streamlines, arising from compression-induced amplification of wall-normal velocity gradients (Eq. 12). This physical-space evolution provides direct visual evidence of the pre-impact turbulence transformation $\Phi^\infty \rightarrow \Phi^{\mathrm{LE}}$ postulated in Section II.

IX. Streamwise Offset Representation of Midspan Profiles

The coupled amplitude and structural evolution of the turbulence field along the midspan probe is visualised in Fig. 12 using an offset representation, in which each wall-normal profile is shifted by its streamwise coordinate and scaled by its global maximum. The plotted abscissa is

$$x_{\mathrm{plot}} = \frac{x}{c} + \frac{q(y;x)}{q_{\max}}, \tag{24}$$

where $q_{\max}$ is the maximum magnitude of quantity q across all stations. This embedding should be read as a qualitative diagnostic of spatial evolution; quantitative comparisons are reserved for the unscaled data.

Far upstream, $\overline{u'u'}$ dominates with a broad wall-normal profile, while the shear stresses $\overline{u'v'}$ and $\overline{u'w'}$ are comparatively small. Approaching the leading edge, $\overline{u'u'}$ decreases systematically while the shear stresses exhibit

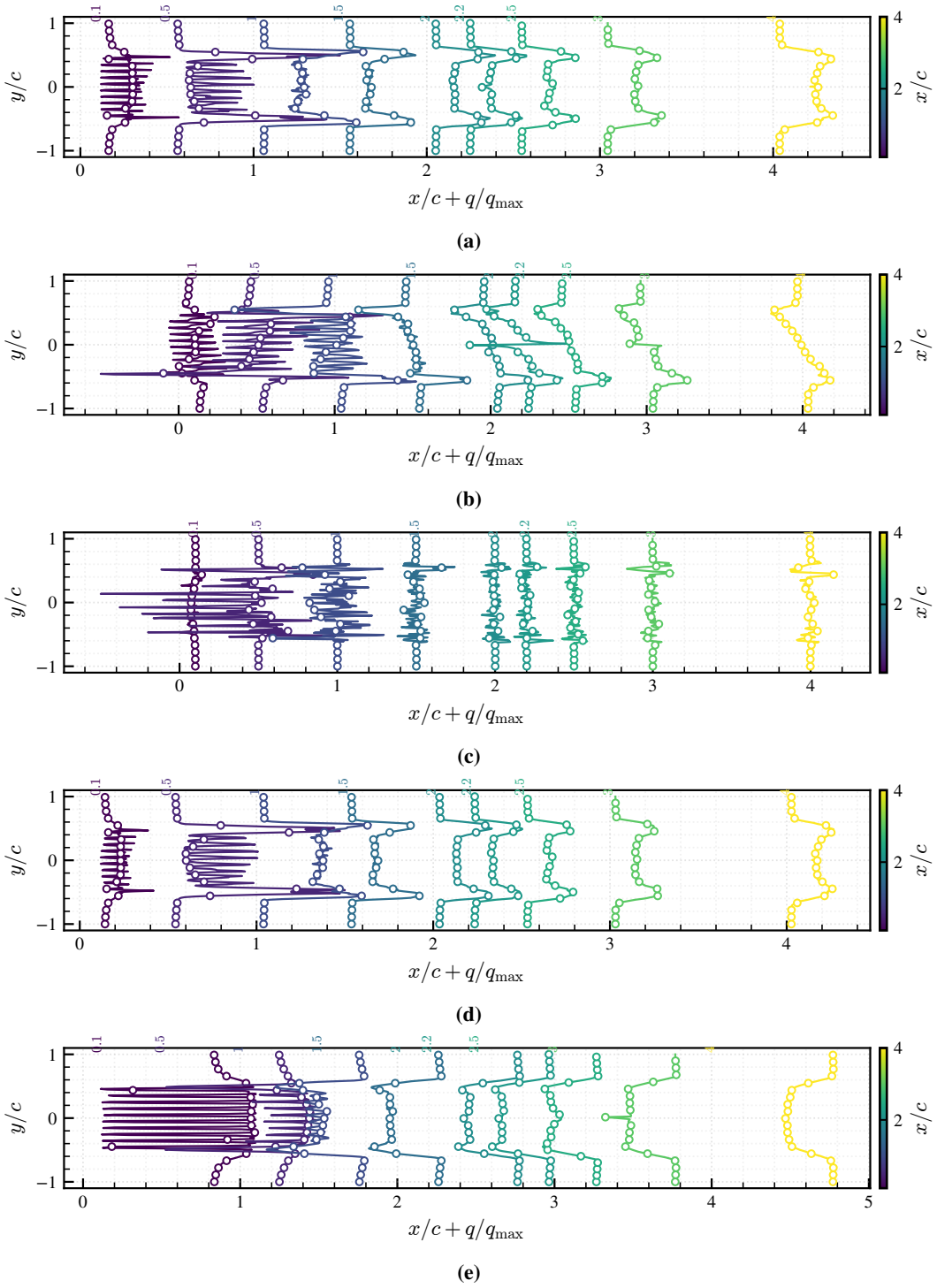

Fig. 12 Streamwise evolution of midspan profiles in offset form. Each profile is shifted by x/c and scaled by the global maximum. Panels correspond to (a) $\overline{u'u'}$; (b) $\overline{u'v'}$; (c) $\overline{u'w'}$; (d) k/U_∞^2; and (e) $|\mathbf{U}|/U_\infty$.

reorganisation including sign changes and spatial localisation, driven by the production term (Eq. 11). The turbulent kinetic energy (Fig. 12d) shows a pronounced upstream maximum followed by sharp, spatially non-uniform decay across the airfoil region, confirming that the distortion process is inherently inhomogeneous and cannot be described by a single scalar attenuation. The smooth variation of the mean velocity magnitude (Fig. 12e) contrasts sharply

with the structured Reynolds-stress evolution, demonstrating that the turbulence changes are not simply convective but are driven by interaction with the mean strain field. The key message of the offset representation is the coupled amplitude-and-structural transformation: energy is redistributed from the dominant streamwise component into shear components and subsequently dissipated, consistent with the tensorial distortion operator of Section II.

X. Pre-Impact Spectral Distortion Near the Leading Edge

A. Patch-based spectral comparison

Spectral tensors are computed from velocity time series on three planar upstream patches and two toroidal patches in the leading-edge pre-impact region. At each vertex, the temporal mean and the instantaneous patch-averaged fluctuation are removed to suppress spatially uniform patch-scale contributions. At each sampling patch P, let N_v denote the number of vertices on the patch. The index j identifies the vertex at which the local time series is evaluated, while m is a summation index over all vertices in the same patch. For each scalar or velocity component $q \in \{u, v, w, p\}$, the temporally averaged value at vertex j is denoted $\overline{q_j}$. The fluctuation used for spectral estimation is then defined as

$$q_j''(t) = q_j(t) - \overline{q_j} - \frac{1}{N_v}\sum_{m=1}^{N_v}\left(q_m(t) - \overline{q_m}\right), \qquad j = 1, \ldots, N_v. \tag{25}$$

One-sided Welch spectra are computed at each vertex and aggregated using a median estimator,

$$\widetilde{\Phi}^{P}_{qq}(f) = \mathrm{median}_{j\in P}\left[\Phi^{(j)}_{qq}(f)\right], \tag{26}$$

and displayed in premultiplied form $f\widetilde{\Phi}_{qq}$ to represent variance per logarithmic frequency decade. A median rather than an arithmetic mean is used because the patch spectra can contain localised high-amplitude vertices associated with near-wall intermittency, geometric clustering, or isolated numerical artefacts. The median therefore provides a robust estimate of the representative patch spectrum and prevents a small number of vertices from dominating the spectral ratio. The mean estimator was also inspected and was found to preserve the same qualitative trends; the median is used here for robustness.

The three upstream planar patches collapse closely across the main resolved frequency range (Fig. 13), establishing spectral stationarity of the incoming turbulence and validating its use as a well-defined reference state. In contrast, the toroidal patches depart systematically from the planar family, with departures that are both frequency-dependent and component-dependent. The most robust feature is attenuation of low-to-intermediate-frequency spectral content on the toroidal surface relative to the upstream reference, combined with a relatively fuller spectral tail at moderate-to-high frequencies near the leading edge. These observations immediately rule out a scalar correction of the form $\Phi^{\mathrm{LE}} = \alpha(f)\Phi^{\infty}$.

B. Scale-dependent spectral gain

The component-wise spectral gain $G_q(f)$ (Eq. 7) is shown in Fig. 14. Four distinct frequency regimes are identified.

Large-scale attenuation. At low frequencies ($f \lesssim 2 \times 10^2$ Hz), all velocity components exhibit $G_q < 1$, indicating suppression of large-scale turbulent motions prior to impact. The wall-normal gain G_v is significantly smaller than G_u and G_w, reflecting the preferential suppression of v' fluctuations by the stagnation-region compression, which is precisely the opposite of the free-space RDT prediction for extensional strains, suggesting the dominance of the wall-blocking effect at large scales.

Intermediate-scale plateau. In the intermediate frequency range, the gains approach a near-flat region, representing the transition zone in which distortion effects from the stagnation strain and geometric blocking partially cancel.

Onset of geometric-scale distortion. A marked increase in G_q is observed near $\kappa \approx 1$, identifying the leading-edge radius as the characteristic geometric scale that controls the spectral transition. This is consistent with the theoretical expectation from Eq. (6) and with the experimental observations of Gill et al. [22].

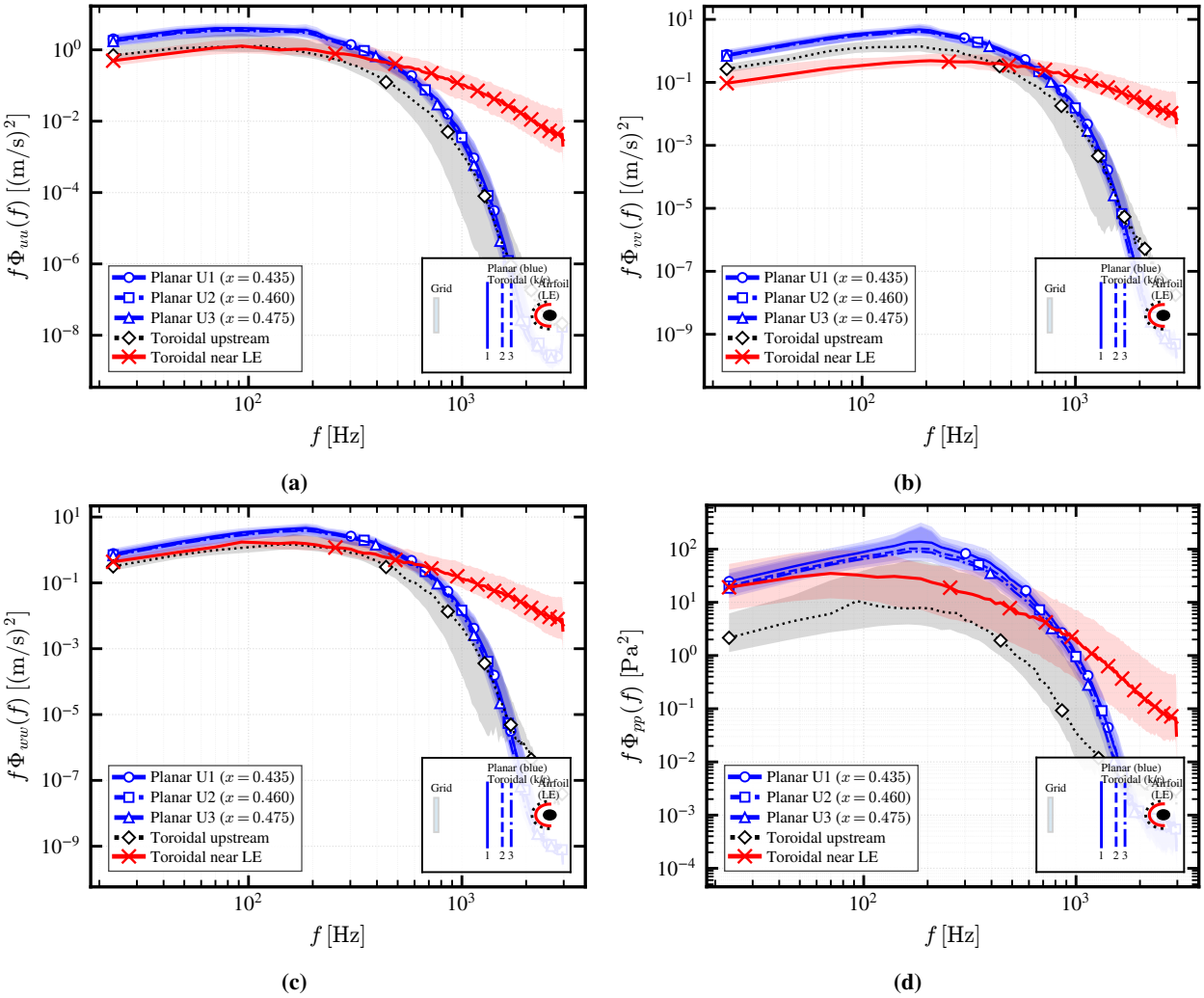

Fig. 13 Premultiplied patch spectra $f\widetilde{\Phi}_{qq}(f)$ for the three planar upstream patches and the two toroidal pre-impact patches: (a) u, (b) v, (c) w, (d) p. The collapse of the upstream planar spectra establishes a stable reference field; the systematic departure of the toroidal spectra from this reference confirms pre-impact distortion.

High-frequency behaviour. At frequencies beyond the $\kappa \approx 1$ transition, apparent amplification is observed, but this regime coincides with rapid decay of the upstream reference spectrum toward the numerical noise floor. The shaded region in Fig. 14 indicates frequencies for which the denominator in Eq. (7) falls below a prescribed reliability threshold; the associated G_q values are not interpreted as physical.

C. Local-frame distortion on toroidal patches

To resolve directional effects relative to the leading-edge curvature, the streamwise and wall-normal velocity components (u, v) are projected onto a local polar frame (r, θ) in the airfoil midspan plane, while the spanwise component remains unchanged as $u_z = w$.

$$u_r = u\cos\theta + v\sin\theta, \qquad u_\theta = -u\sin\theta + v\cos\theta, \qquad u_z = w. \tag{27}$$

where θ is the azimuthal coordinate around the toroidal patch. This projection is orthogonal in the (y, z)-plane, preserving the cross-plane trace,

$$\Phi_{uu} + \Phi_{vv} = \Phi_{rr} + \Phi_{\theta\theta}, \qquad \Phi_{zz} = \Phi_{ww}. \tag{28}$$

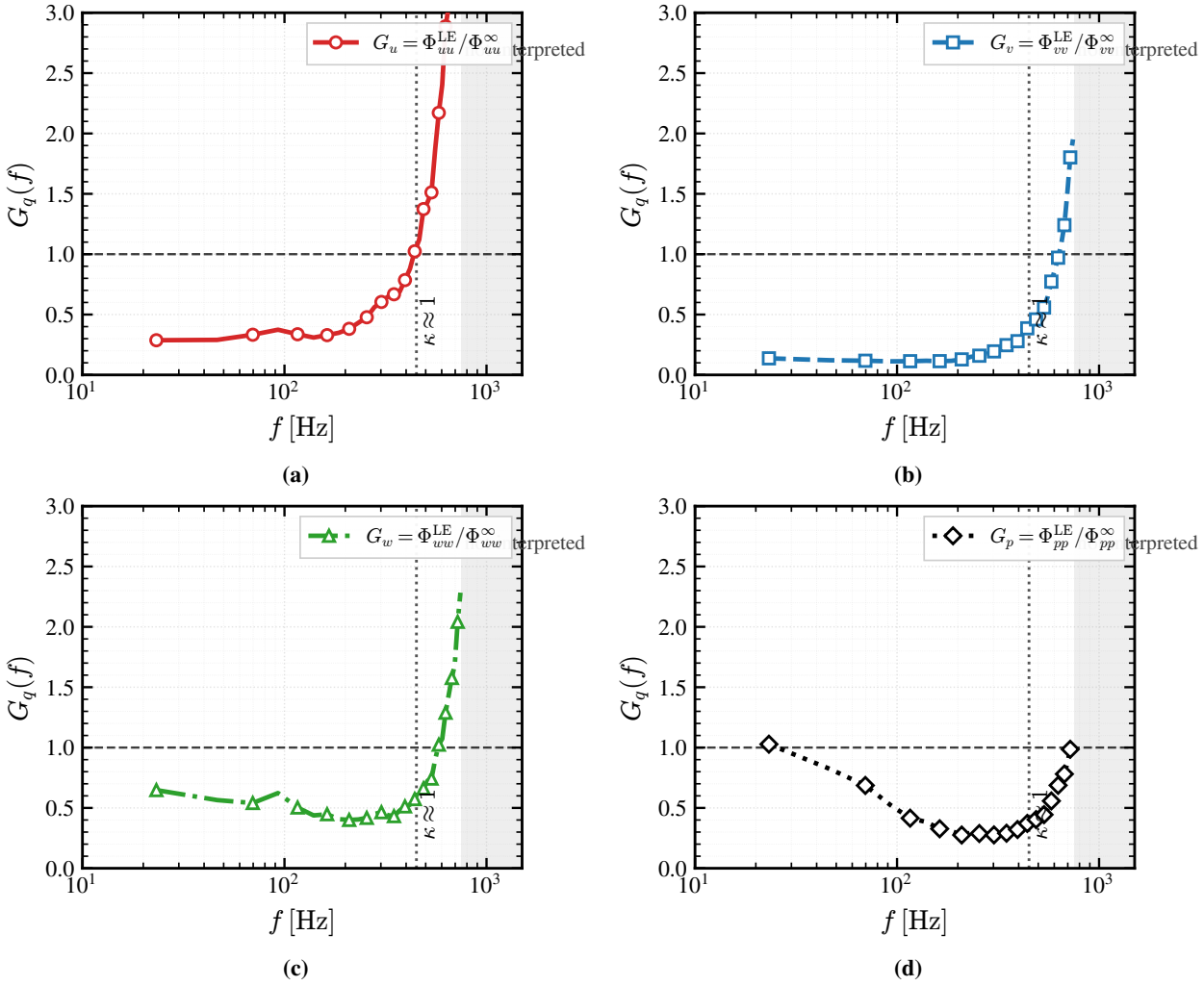

Fig. 14 Component-wise spectral gains $G_q(f) = \Phi^{\mathrm{LE}}_{qq}/\Phi^{\infty}_{qq}$ for (a) u, (b) v, (c) w, and (d) p. The dashed horizontal line marks $G_q = 1$ and the vertical marker indicates $\kappa \approx 1$. Shaded regions denote frequencies where the upstream spectrum is below the reliability threshold; these are not interpreted.

Any difference between Φ_{rr} and $\Phi_{\theta\theta}$ therefore reflects genuine directional redistribution of turbulent energy. The local distortion is quantified as

$$\Delta_{qq}(St,\theta) = \log_{10}\left(\frac{\widetilde{\Phi}^{\mathrm{LE}}_{qq}(St,\theta)}{\widetilde{\Phi}^{\mathrm{Up}}_{qq}(St,\theta)}\right), \quad q \in \{r,\theta\}, \tag{29}$$

with premultiplied spectra $\widetilde{\Phi}_{qq} = St\,\Phi_{qq}$.

The distortion maps (Fig. 15) reveal a monotonic increase of Δ_{qq} with St for both components: large-scale motions are predominantly attenuated ($\Delta < 0$), while smaller-scale motions are relatively amplified ($\Delta > 0$), with the transition occurring near $St = O(8\text{–}10)$. A systematic difference between components is present: Δ_{rr} exhibits stronger amplification at moderate-to-high St than $\Delta_{\theta\theta}$, indicating that radial (wall-normal) fluctuations are preferentially enhanced at scales near $\kappa \approx 1$, while azimuthal (tangential) fluctuations remain comparatively weaker. The angular dependence of Δ_{qq} is non-trivial and does not follow a simple monotonic trend in θ, indicating modulation by the local mean-flow topology around the nose, including asymmetry between the pressure and suction sides.

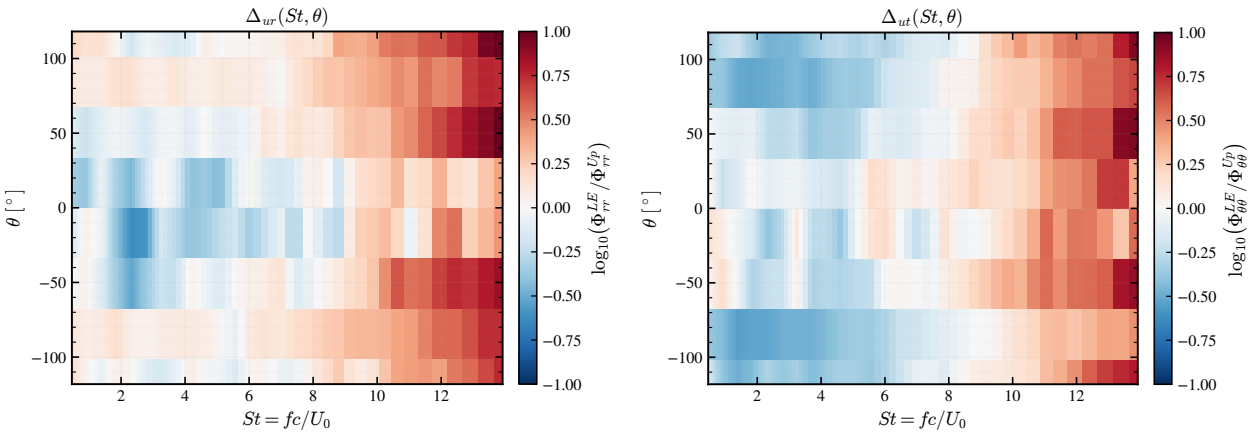

(a) $\Delta_{rr}(St,\theta)$. **(b)** $\Delta_{\theta\theta}(St,\theta)$.

Fig. 15 Local-frame distortion maps after projecting $(v,w) \mapsto (u_r, u_\theta)$ via Eq. (27). The systematic difference between Δ_{rr} and $\Delta_{\theta\theta}$ confirms component-dependent distortion consistent with a tensorial operator $\mathcal{D}(\kappa,\theta)$.

D. Cross-plane energy diagnostics

Three reduced diagnostics are introduced to separate total cross-plane energy modification from directional redistribution within the cross-plane.

Azimuth-averaged distortion. Averaging Δ_{qq} over θ (Fig. 16(a)) confirms that both components remain near-neutral or weakly attenuated at low St and exhibit rapid amplification beyond $St = O(10)$, with $\overline{\Delta}_{rr}$ consistently exceeding $\overline{\Delta}_{\theta\theta}$.

Trace gain. The cross-plane trace gain

$$G_\perp(St,\theta) = \frac{\widetilde{\Phi}_{rr}^{\mathrm{LE}} + \widetilde{\Phi}_{\theta\theta}^{\mathrm{LE}}}{\widetilde{\Phi}_{rr}^{\mathrm{Up}} + \widetilde{\Phi}_{\theta\theta}^{\mathrm{Up}}} \tag{30}$$

is invariant under rotations in the (y,z)-plane and therefore isolates the net cross-plane energy change. Figure 16(b) shows that the onset of net amplification occurs over a narrow St range with weak θ-dependence, suggesting a geometric filtering mechanism controlled by r_{LE}.

Cross-plane anisotropy change. The anisotropy parameter

$$\chi = \frac{\Phi_{rr} - \Phi_{\theta\theta}}{\Phi_{rr} + \Phi_{\theta\theta}}, \qquad \Delta\chi = \chi^{\mathrm{LE}} - \chi^{\mathrm{Up}}, \tag{31}$$

distinguishes radial-dominated ($\chi > 0$) from azimuthal-dominated ($\chi < 0$) states independently of the energy level. The angular variation of $\Delta\chi$ (Fig. 16(c)) is pronounced and sign-changing at higher St, confirming that the directional redistribution of cross-plane energy is not azimuthally symmetric, and must be described as a function of both κ and θ.

E. Implications for leading-edge noise modelling

The spectral and directional evidence presented in this section leads to a single overarching conclusion: the turbulence field incident on the airfoil surface in Amiet-type and related formulations [1, 2, 13, 26] is not equivalent to the undistorted upstream spectrum. Between the upstream reference plane and the toroidal pre-impact surface, the turbulence spectrum is modified in amplitude, frequency content, component distribution, and azimuthal structure. The leading-edge region therefore imposes a measurable, scale-dependent, and component-dependent pre-impact transformation on the incoming turbulence before acoustic scattering occurs. The pipeline for leading-edge noise modelling must be recast to include an explicit distortion stage:

$$\Phi_{ij}^{\infty}(\kappa,\theta) \xrightarrow{\mathcal{D}_{ijmn}(\kappa,\theta)} \Phi_{ij}^{\mathrm{LE}}(\kappa,\theta) \xrightarrow{\text{acoustic scattering}} S_{pp}(f), \tag{32}$$

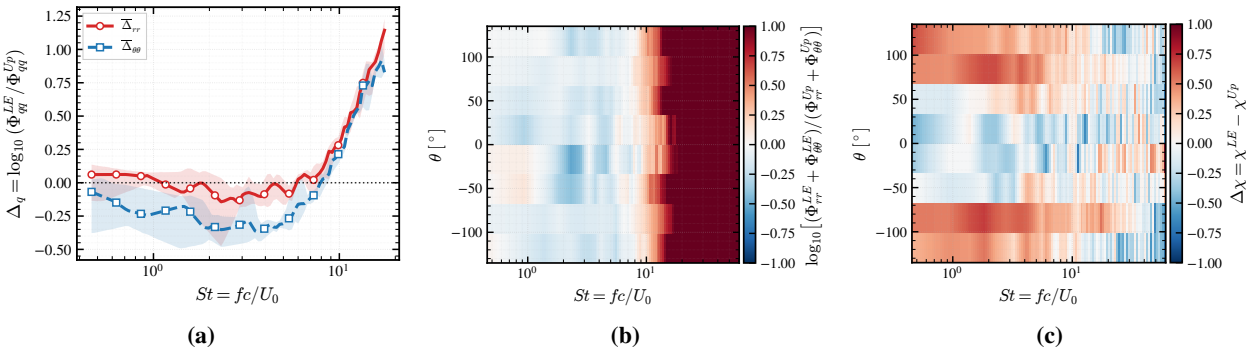

Fig. 16 Reduced cross-plane distortion diagnostics: (a) azimuth-averaged distortion $\overline{\Delta}_{rr}$ and $\overline{\Delta}_{\theta\theta}$; (b) cross-plane trace gain $G_\perp(St, \theta)$; (c) cross-plane anisotropy change $\Delta\chi(St, \theta)$.

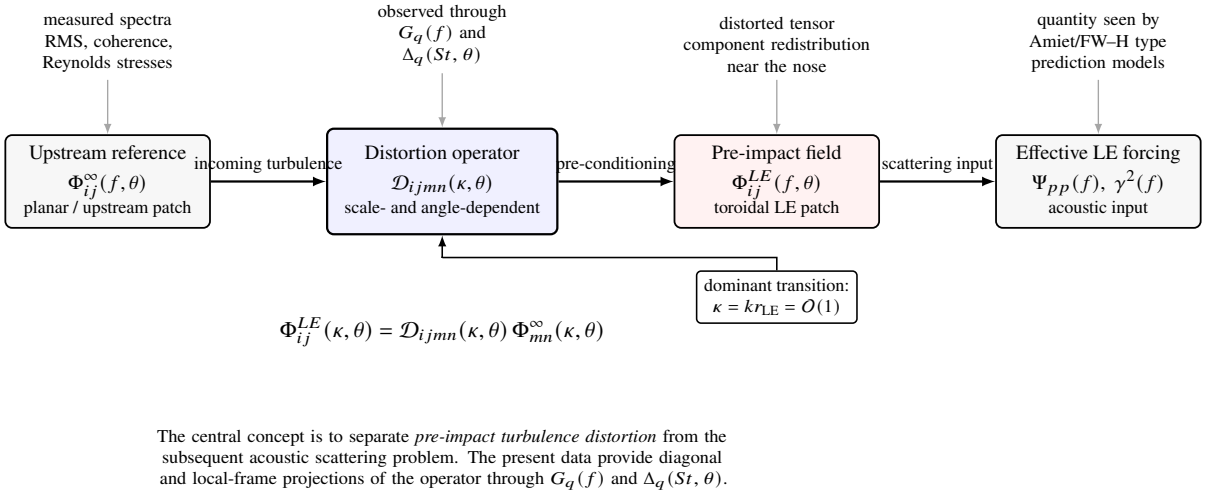

The central concept is to separate *pre-impact turbulence distortion* from the subsequent acoustic scattering problem. The present data provide diagonal and local-frame projections of the operator through $G_q(f)$ and $\Delta_q(St, \theta)$.

Fig. 17 Schematic of the proposed distortion-operator framework. The upstream spectral tensor is transformed by a scale- and azimuth-dependent operator $\mathcal{D}$ before entering the leading-edge acoustic scattering problem. The present study characterises $\mathcal{D}$ empirically through spectral gain and local-frame distortion diagnostics.

as illustrated schematically in Fig. 17. The present data provide the diagonal and azimuthally projected components of $\mathcal{D}$ through $G_q(f)$ and $\Delta_q(St, \theta)$. Reconstruction of the full tensor requires projection into a true surface-aligned (t, n, z) frame and resolution studies for the high-St spectral tail; these are subjects of ongoing work.

XI. Conclusion

This work has demonstrated, through high-fidelity lattice Boltzmann simulations of turbulence interacting with a NACA 0012 airfoil at $Re_c \approx 5.1 \times 10^5$, that the turbulence field undergoes a systematic, physically significant, and aeroacoustically consequential transformation before impacting the leading edge. The principal findings are as follows.

Turbulence distortion is a physical reality. The combination of instantaneous vorticity fields, Reynolds-stress budgets, and Lumley invariant trajectories establishes beyond doubt that the turbulence state in the pre-impact region is fundamentally different from that at the upstream reference location. The transformation is not attributable to free-space decay alone, but is driven by the stagnation-region mean strain field, which compresses fluid elements in the wall-normal direction and stretches them tangentially, in agreement with rapid distortion theory [16, 18].

The transformation is tensorial and irreversible. Reynolds-stress analysis shows that component-to-component ratios change substantially approaching the leading edge, ruling out a scalar or isotropic correction. The Lumley

invariant trajectory exhibits a transient eigenvalue reordering (excursion toward $III < 0$) that cannot be captured by linear scaling and is indicative of pressure–strain redistribution [43]. Downstream of the airfoil, the stress tensor does not recover its upstream anisotropy state, confirming irreversible distortion.

The distortion is scale-dependent and controlled by $\kappa = kr_{\mathrm{LE}}$. Spectral gains $G_q(f)$ computed between the upstream reference and the toroidal pre-impact surface are frequency-dependent and component-dependent, with large-scale motions ($\kappa \lesssim 1$) attenuated and the transition to a different spectral regime occurring near $\kappa \approx 1$. The leading-edge radius r_{LE} therefore acts as a geometric filter that separates turbulent scales into strongly and weakly distorted classes, consistent with the operator formulation of Section II.

Directional redistribution is azimuthally non-uniform. Local-frame distortion maps $\Delta_{qq}(St, \theta)$ and the cross-plane anisotropy diagnostic $\Delta\chi(St, \theta)$ reveal that the transformation is not axisymmetric. The radial component (aligned with the local surface normal) is preferentially enhanced relative to the azimuthal component, and the angular dependence of the redistribution is modulated by the nose geometry and mean-flow topology on the pressure and suction sides.

Implications for predictive models. These results establish turbulence distortion as a necessary pre-conditioning stage in leading-edge noise prediction. The appropriate modelling pipeline is not $\Phi^{\infty} \rightarrow S_{pp}(f)$, but the two-stage process described in Eq. (32): $\Phi^{\infty} \rightarrow \mathcal{D} \rightarrow \Phi^{\mathrm{LE}} \rightarrow S_{pp}(f)$. Amiet-type models that use the undistorted upstream spectrum as direct input to the acoustic transfer function will systematically underestimate the structural modification of the turbulence field and may require additional correction terms that implicitly approximate $\mathcal{D}$. The present work provides the first explicit data-driven characterisation of the operator components $G_q(f)$ and $\Delta_q(St, \theta)$.

Outlook. The full reconstruction of $\mathcal{D}_{ijmn}(\kappa, \theta)$ requires projection of the velocity field onto a consistent surface-aligned (t, n, z) frame, independent measurement of the convection velocity $U_c(f, \theta)$ to resolve the temporal-to-spatial spectral conversion, and resolution studies for the high-κ tail. Future work will investigate the parametric dependence of $\mathcal{D}$ on airfoil geometry (leading-edge radius, camber, thickness) and inflow conditions (turbulence intensity, integral scale), with the aim of constructing a reduced-order distortion model suitable for integration into existing semi-analytical LE noise prediction frameworks.

Acknowledgements

The authors gratefully acknowledge the use of the CARO high-performance computing facility (Computer for Advanced Research in Aerospace) at the German Aerospace Center (DLR). This study was conducted within the DLR project *Exergie*.

References

[1] Amiet, R. K., "Acoustic radiation from an airfoil in a turbulent stream," *J. Sound Vib.*, Vol. 41, No. 4, 1975, pp. 407–420. https://doi.org/https://doi.org/10.1016/S0022-460X(75)80105-2.

[2] Glegg, S. A. L., and Devenport, W. J., "Panel methods for airfoils in turbulent flow," *J. Sound Vib.*, Vol. 329, No. 18, 2010, pp. 3709–3720. https://doi.org/https://doi.org/10.1016/j.jsv.2010.03.007.

[3] Moriarty, P., Guidati, G., and Migliore, P., "Prediction of Turbulent Inflow and Trailing-Edge Noise for Wind Turbines," *11th AIAA/CEAS Aeroacoustics Conf.*, American Institute of Aeronautics and Astronautics, Reston, Virigina, 2005. https://doi.org/https://doi.org/10.2514/6.2005-2881.

[4] Kim, J. W., Haeri, S., and Joseph, P. F., "On the reduction of aerofoil–turbulence interaction noise associated with wavy leading edges," *Journal of Fluid Mechanics*, Vol. 792, 2016, pp. 526–552. https://doi.org/10.1017/jfm.2016.95.

[5] Paterson, R. W., and Amiet, R. K., "Acoustic Radiation and Surface Pressure Characteristics of an Airfoil due to Incident Turbulence," *NASA Cr-2733*, 1976, p. 571. https://doi.org/doi:10.2514/6.1976-571.

[6] Paterson, R. W., and Amiet, R. K., "Noise of a model helicopter rotor due to ingesting turbulence," Tech. Rep. NASA TM-78525, NASA, 1979.

[7] Olsen, W., and Wagner, J., "Effect of thickness on airfoil surface noise," *AIAA Journal*, Vol. 20, No. 3, 1982, pp. 437–439. https://doi.org/10.2514/3.7922, URL https://arc.aiaa.org/doi/10.2514/3.7922.

[8] Lockard, D. P., and Morris, P. J., "Radiated Noise from Airfoils in Realistic Mean Flows," *AIAA Journal*, Vol. 36, No. 6, 1998, pp. 907–914. https://doi.org/10.2514/3.13912.

[9] Glegg, S. A. L., and Devenport, W., "Unsteady Loading on an Airfoil of Arbitrary Thickness," *Journal of Sound and Vibration*, Vol. 319, No. 3–5, 2009, pp. 1252–1270. https://doi.org/10.1016/j.jsv.2008.06.053.

[10] Hall, A. M., Atassi, O. V., Gilson, J., Reba, R., and Shannon, D., "Effect of Leading-Edge Thickness on High-Speed Airfoil-Turbulence Interaction Noise," *17th AIAA/CEAS Aeroacoustics Conference*, Portland, Oregon, 2011. https://doi.org/10.2514/6.2011-2861.

[11] Sharma, S., Sarradj, E., and Schmidt, H., "Stochastic modelling of leading-edge noise in time-domain using vortex particles," *Journal of Sound and Vibration*, Vol. 488, 2020, p. 115656. https://doi.org/10.1016/j.jsv.2020.115656.

[12] Sharma, S., and Herr, M., "Efficient Prediction of Turbulent Inflow and Leading-Edge Interaction Noise Using a Vortex Particle Method with Look-up Table Approach," *Journal of Physics: Conference Series*, Vol. 2767, 2024, p. 022059. https://doi.org/10.1088/1742-6596/2767/2/022059.

[13] Piccolo, A., Zamponi, R., Avallone, F., and Ragni, D., "Turbulence distortion and leading-edge noise," *Physics of Fluids*, Vol. 36, No. 12, 2024, p. 125183. https://doi.org/10.1063/5.0244627.

[14] Gershfeld, J., "Leading edge noise from thick foils in turbulent flows," *J. Acoust. Soc. Am.*, Vol. 116, No. 3, 2004, pp. 1416–1426. https://doi.org/https://doi.org/10.1121/1.1780575.

[15] Lysakn, P. D., Capone, D. E., and Jonson, M. L., "Prediction of high frequency gust response with airfoil thickness effects," *Journal of Fluids and Structures*, Vol. 39, 2013, pp. 258–274. https://doi.org/10.1016/j.jfluidstructs.2013.02.006.

[16] Batchelor, G. K., *The Theory of Homogeneous Turbulence*, Cambridge University Press, 1953. https://doi.org/10.1017/CBO9780511607919.

[17] Goldstein, M. E., *Aeroacoustics*, McGraw-Hill International Book Co, 1976.

[18] Hunt, J. C. R., and Carruthers, D. J., "Rapid distortion theory and the 'problems' of turbulence," *Journal of Fluid Mechanics*, Vol. 212, 1990, pp. 497–532. https://doi.org/10.1017/S0022112090002075.

[19] Guidati, G., Bareiss, R., Wagner, S., and Parchen, R., "Simulation and Measurement of Inflow-Turbulence Noise on Airfoils," *3rd AIAA/CEAS Aeroacoustics Conference*, 1997. https://doi.org/10.2514/6.1997-1698.

[20] Guidati, G., and Wagner, S., "Prediction of airfoil noise in compressible turbulent flows," *4th AIAA/CEAS Aeroacoustics Conf.*, American Institute of Aeronautics and Astronautics, Reston, Virigina, 1998. https://doi.org/https://doi.org/10.2514/6.1998-2227.

[21] Moriarty, P., "Development and Validation of a Semi-Empirical Wind Turbine Aeroacoustic Code," *42nd AIAA Aerospace Sciences Meeting and Exhibit*, American Institute of Aeronautics and Astronautics, Reston, Virigina, 2004. https://doi.org/https://doi.org/10.2514/6.2004-1189.

[22] Gill, J., Zhang, X., and Joseph, P., "Symmetric airfoil geometry effects on leading edge noise." *The Journal of the Acoustical Society of America*, Vol. 134, 2013, pp. 2669–2680. https://doi.org/10.1121/1.4818769, URL http://www.ncbi.nlm.nih.gov/pubmed/24116405.

[23] Bowen, L., Celik, A., Azarpeyvand, M., and da Silva, C. R., "Grid Generated Turbulence for Aeroacoustic Facility," *AIAA Journal*, Vol. 60, 2022, pp. 1833–1847. https://doi.org/10.2514/1.J060851.

[24] Trascinelli, L., Bowen, L., Piccolo, A., Avallone, F., Zamponi, R., Ragni, D., Zang, B., and Zhou, B. Y., "Numerical Simulation of Grid-Generated Turbulence Interaction with a NACA0012 Airfoil," American Institute of Aeronautics and Astronautics (AIAA), 2023. https://doi.org/10.2514/6.2023-3633.

[25] Kim, J. W., and Haeri, S., "An Advanced Synthetic Eddy Method for the Computation of Aerofoil–Turbulence Interaction Noise," *Journal of Computational Physics*, Vol. 287, 2015, pp. 1–17. https://doi.org/10.1016/j.jcp.2015.01.039.

[26] dos Santos, F. L., Botero-Bolívar, L., Venner, C. H., and de Santana, L. D., "Inflow turbulence distortion for airfoil leading-edge noise prediction for large turbulence length scales for zero-mean loading," *The Journal of the Acoustical Society of America*, Vol. 153, No. 3, 2023, pp. 1811–1822. https://doi.org/10.1121/10.0017458.

[27] ProLB, https://www.prolb-cfd.com/, 2025.

[28] Djenidi, L., "Lattice-Boltzmann simulation of grid-generated turbulence," *Journal of Fluid Mechanics*, Vol. 552, 2006, pp. 13–35. https://doi.org/10.1017/S002211200600869X.

[29] Smagorinsky, J., "General circulation experiments with the primitive equations: I. The basic experiment," *Mon. Weather Rev.*, Vol. 91, No. 3, 01 Mar. 1963, pp. 99 – 164. https://doi.org/10.1175/1520-0493(1963)091<0099:GCEWTP>2.3.CO;2.

[30] Herr, M., Ewert, R., Rautmann, C., Kamruzzaman, M., Bekiropoulos, D., Arina, R., Iob, A., Batten, P., Chakravarthy, S., and Bertagnolio, F., "Broadband Trailing-Edge Noise Predictions—Overview of BANC-III Results," *21st AIAA/CEAS Aeroacoustics Conference*, American Institute of Aeronautics and Astronautics, Dallas, TX, 2015. https://doi.org/10.2514/6.2015-2847.

[31] Welch, P., "The use of fast Fourier transform for the estimation of power spectra: a method based on time averaging over short, modified periodograms," *IEEE Trans. Audio Electroacoust.*, Vol. 15, No. 2, 1967, pp. 70–73.

[32] del Álamo, J. C., and Jiménez, J., "Estimation of turbulent convection velocities and corrections to Taylor's approximation," *Journal of Fluid Mechanics*, Vol. 640, 2009, pp. 5–26. https://doi.org/10.1017/S0022112009991029.

[33] Comte-Bellot, G., and Corrsin, S., "Simple Eulerian time correlation of full- and narrow-band velocity signals in grid-generated, 'isotropic' turbulence," *Journal of Fluid Mechanics*, Vol. 48, No. 2, 1971, pp. 273–337. https://doi.org/10.1017/S0022112071001599.

[34] Roach, P. E., "The generation of nearly isotropic turbulence by means of grids," *International Journal of Heat and Fluid Flow*, Vol. 8, No. 2, 1987, pp. 82–92. https://doi.org/10.1016/0142-727X(87)90001-4.

[35] Durbin, P. A., and Reif, B. A. P., *Statistical Theory and Modeling for Turbulent Flows*, 2nd ed., John Wiley & Sons, 2017. https://doi.org/10.1002/9781119231414.

[36] Taylor, G. I., "The Spectrum of Turbulence," *Proceedings of the Royal Society of London. Series A*, Vol. 164, No. 919, 1938, pp. 476–490.

[37] Wyngaard, J. C., and Clifford, S. F., "Taylor's Hypothesis and High-Frequency Turbulence Spectra," *Journal of the Atmospheric Sciences*, Vol. 34, No. 6, 1977, pp. 922–929. https://doi.org/10.1175/1520-0469(1977)034<0922:THAHTS>2.0.CO;2.

[38] Ertunç, Ö., Özyilmaz, N., Lienhart, H., Durst, F., and Beronov, K., "Homogeneity of turbulence generated by static-grid structures," *Journal of Fluid Mechanics*, Vol. 654, 2010, pp. 473–500. https://doi.org/10.1017/S0022112010000479.

[39] Sreenivasan, K. R., and Antonia, R. A., "The Phenomenology of Small-Scale Turbulence," *Annual Review of Fluid Mechanics*, Vol. 29, No. 1, 1997, pp. 435–472. https://doi.org/10.1146/annurev.fluid.29.1.435.

[40] Pope, S. B., *Turbulent Flows*, Cambridge Univ. Press, 2000.

[41] Lumley, J. L., and Newman, G. R., "The return to isotropy of homogeneous turbulence," *Journal of Fluid Mechanics*, Vol. 82, No. 1, 1977, p. 161–178. https://doi.org/10.1017/S0022112077000585.

[42] Banerjee, S., Krahl, R., Durst, F., and Zenger, C., "Presentation of anisotropy properties of turbulence, invariants versus eigenvalue approaches," *Journal of Turbulence*, Vol. 8, 2007, pp. 1–27. https://doi.org/10.1080/14685240701506896.

[43] Speziale, C. G., Sarkar, S., and Gatski, T. B., "Modelling the pressure–strain correlation of turbulence: an invariant dynamical systems approach," *Journal of Fluid Mechanics*, Vol. 227, 1991, pp. 245–272. https://doi.org/10.1017/S0022112091000101.